Comparison of nanosecond pulsed discharges in water for different pulse polarities

Bachelor Thesis

in the
Degree Program
“Bachelor of Science“
in Physics

at the Faculty of Physics and Astronomy
of the Ruhr-Universität Bochum

by
Marina Falke

from
Münster

Bochum (2021)

Abstract

In-liquid plasmas generated by high-voltage pulses offer a wide range of possible applications, including water treatment, plasma medicine and nanoparticle production. Unlike plasmas with voltage rise times higher than a few nanoseconds no gas bubble can be formed prior the discharge and the liquid cannot react to the pressure difference due to its inertia. Therefore, various models have been developed to describe the ignition process and following plasma propagation. Possible propagation media are supercritical fluids and so-called nanovoids, which are microscopic low density regions created due to electrostriction caused by the high electric field strength. In both models, however, the formation of the initial electrons is not explained. These electrons can be created by field effects at the electrode-water interface. Although these hypotheses are supported by theory, experimental data are sparse due to the very fast processes appearing on a small spatial scale. In this work, the ignition of nanosecond high-voltage pulsed discharges in distilled water is analysed using ICCD imaging and optical emission spectroscopy for different pulse polarities. For this purpose, different electrode materials (W, Pt, Pt/Ir) with voltage amplitudes ranging from 16 kV to 26 kV were used. In addition, scanning electron microscopy was used to investigate the surface structure of the electrode tips before and after plasma ignition. The analysis of the emission spectra shows differences between positive and negative pulse polarity, which can be explained by field ionisation and field emission, respectively. Black body emission can be fitted to the spectra resulting in surface temperatures of 7000 K for positive polarity and significantly lower temperatures for negative polarity. During ignition the light evolution is higher for the positive pulse than for the negative pulse. This is related to the electron density evolution, which reaches values of $4 \times 10^{25}\,\mathrm{m}^{-3}$ for positive polarity and $2 \times 10^{25}\,\mathrm{m}^{-3}$ for negative polarity. During plasma propagation both polarities show formation of similar streamer branches and an identical electron density. Therefore, the ignition of the plasma can be explained by material- and polarity-dependent field effects in combination with plasma propagation in a region of low density. These regions of low density can be caused by density fluctuations in water in the supercritical state or by nanovoids.

Zusammenfassung

Durch Hochspannungspulse erzeugte Plasmen in Flüssigkeiten bieten ein breites Spektrum von Anwendungsmöglichkeiten, unter anderem in der Wasserbehandlung, der Plasmamedizin und der Nanopartikelherstellung. Im Gegensatz zu Plasmen mit Spannungsanstiegszeiten, die größer als einige Nanosekunden sind, kann sich vor der Entladung keine Gasblase bilden und die Flüssigkeit aufgrund ihrer Trägheit nicht auf den Druckunterschied reagieren. Da deswegen eine Kavitationsblasenbildung vor der Entladung nicht möglich ist, wurden verschiedene Modelle entwickelt, um Zünd- und Ausbreitungsmechanismen zu beschreiben. In Frage kommende Ausbreitungsmedien sind überkritische Flüssigkeiten und so genannte Nanoporen, mikroskopisch kleine Regionen mit geringer Dichte, die durch Elektrostriktion aufgrund des hohen elektrischen Feldes entstehen. Bei beiden Modellen ist jedoch keine Erklärung für die Entstehung der ersten Elektronen erhalten. Diese könnten durch Feldeffekte gefolgt von tunnelnden Elektronen zwischen dem Material der Elektrodenspitzen und der umgebenden Flüssigkeit verursacht werden. Obwohl die Hypothesen durch die Theorie unterstützt werden, existieren kaum experimentelle Daten aufgrund der sehr schnellen und räumlich begrenzten Prozesse. In dieser Arbeit wird die Zündung eines Nanosekunden-Hochspannungspulses in destilliertem Wasser mittels ICCD-Aufnahmen und optischer Emissionsspektroskopie für verschiedene Pulspolaritäten analysiert. Dazu wurden verschiedene Elektrodenmaterialien (W, Pt, Pt/Ir) und Spannungsamplituden von 16 kV bis 26 kV verwendet. Zusätzlich wurde mit Hilfe der Rasterelektronenmikroskopie die Oberflächenstruktur der Elektrodenspitzen vor und nach der Plasmazündung untersucht. Die Analyse der Emissionsspektren zeigt Unterschiede zwischen positiver und negativer Pulspolarität, die durch Feldionisation bei positiver Elektrodenpolarität und Feldemission bei negativer Polarität erzeugt werden. Die Schwarzkörperemission kann an die Spektren angepasst werden, was zu Oberflächentemperaturen von 7000 K für positive Polarität und deutlich niedrigeren Temperaturen für negative Polarität führt. Auch der Verlauf der Lichtintensität bei der Zündung ist für den positiven Spannungspuls höher als beim negativen Puls. Dies steht im Zusammenhang mit der Entwicklung der Elektronendichte, die bei der positiven Polarität Werte von $4 \times 10^{25}\,\mathrm{m}^{-3}$ und bei der negativen Polarität Werte von nur nur $2 \times 10^{25}\,\mathrm{m}^{-3}$ erreicht. Während der Plasmaausbreitung sind dann sowohl Form der Streamer als auch die Elektronendichte für beide Polaritäten identisch. Deswegen wird die Zündung des Plasmas mit material- und polaritätsabhängigen Feldeffekten in Kombination mit einer Plasmaausbreitung in einer Region mit geringer Dichte erklärt. Diese Regionen geringer Dichte können sowohl durch Dichtefluktuationen bei Wasser im überkritischen Zustand als auch durch Nanoporen erklärt werden.

Contents

1 Motivation

Since S. Whitehead published the first paper on plasmas ignited directly inside liquids in 1928 [1], it has become an increasingly important field of research [2]. In the meantime, numerous setups and applications for plasmas in or in contact with liquids have been developed. The most common applications nowadays are the production of nanoparticles [3, 4], the treatment of wastewater [5–8], the use of plasmas in/in contact with liquids in medicine [9–11] or for surface treatment [12, 13].

One promising application in future chemistry, biomedicine and industry is the growth of copper oxide nanoparticles on copper substrates. These copper oxide substrates are required as catalysts for the electrochemical conversion of carbon dioxide. During the application of these catalysts, the copper surface wears off and the catalytic ability decreases. The goal is therefore to reactivate and enlarge the surface structure by treating the copper substrates with pulsed plasmas within an electrochemical cell [13]. In this way, carbon dioxide could be reduced more effectively into carbon monoxide and converted into solar fuels, which is of increasing importance in the context of the rising global temperature and the threat of climate change.

Furthermore, plasmas in and in contact with liquid find application as advanced oxidation processes (AOP) for water purification [5]. With plasmas in water a simultaneous introduction of ionised gas in higher amounts is possible. Thus, the concentration of organic contaminants can be degraded by OH radicals [6]. The OH radicals can be a solution to remove chlorine resistant bacteria from the water [5]. It is not possible for bacteria to develop resistance against the chemical oxidation of the microbial structure. Therefore, water treatment with in-liquid plasmas is a potential revolution in waste water treatment and drinking water production [5, 6].

The physical processes underlying plasma discharges in water are still not fully understood [14]. Ignition and propagation of the plasma are both still under discussion as well as the induced chemistry. While the ignition mechanism for pulses with rise times longer than tens of nanoseconds has already been scientifically clarified, the ignition for pulses with very short rise times not longer than a few nanoseconds, is subject of discussions. For longer rise times, the liquid can react to the high electric field and the pressure differences caused by it [2], Ohmic heating occurs and the liquid evaporates. The plasma then ignites inside this gaseous bubble. If short rise times in

order of few nanoseconds are considered, the inertia of water is too large to react to the pressure difference. Ignition only due to electron collision ionisation is not possible [15]. Another physical effect must cause the ignition of nanosecond pulsed plasmas in liquid surroundings.

The aim of this work is therefore to verify or falsify the currently existing theoretical models [16, 17] by experimental observations. Special attention is thereby paid to the aspect of plasma ignition in distilled water. For this purpose, plasma discharges generated by nanosecond high-voltage (HV) pulses are observed through different methods and compared for different properties. Special attention is paid to the comparison of negative polarity in contrast to positive polarity. Furthermore, the electrode material used and the level of the applied voltage are varied.

The optical methods used also vary from shadowgraphy and intensified charge-coupled device (ICCD) imaging to optical emission spectroscopy (OES). ICCD photography is used to study the intensity evolution and streamer formation and compare them with the shape of the voltage pulse measured by an oscilloscope. Meanwhile, shadowgraphy provides information about the dissipated energy and OES supplies data about the electron densities, the emitted H_α light and the temperature of the electrode surface. This is directly related to the observation of the electrode surfaces for different materials before and after exposure to the plasma.

The knowledge about the discharge behaviour on different materials and the variation of the voltage strength and polarity contribute to the overall understanding of the discharge behavior of nanosecond HV plasmas in liquids.

2 Theoretical Background

The physical processes causing plasma ignition and propagation in liquid environments are very challenging to study, as they involve plasma physics, thermodynamics, hydrodynamics, quantum mechanics and gas-liquid-solid interactions [12]. Therefore, the most important theoretical foundations are laid in this chapter, whereby the focus is placed on the fundamentals of nanosecond high-voltage pulsed plasmas in distilled water for a pin-to-pin electrode configuration. Section 2.1, deals with the evolution of the discharge and the hydrodynamic reaction of the liquid. In section 2.2 the models that could explain direct ignition of the plasma in the liquid are described.

2.1 Plasmas in Liquids

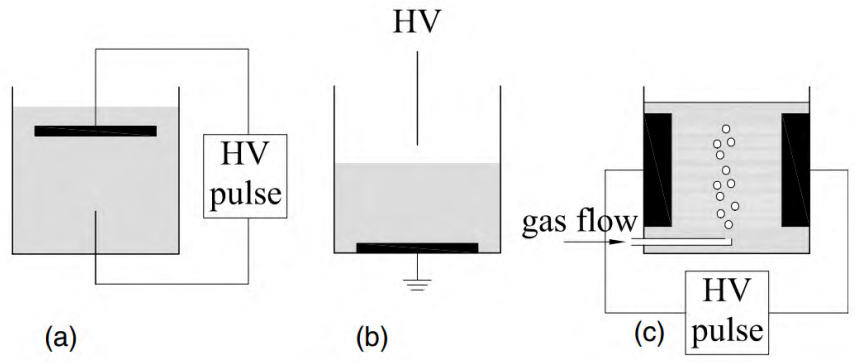

Figure 1. Examples of electrode configurations: (a) Discharge directly inside liquid, (b) gas phase discharge with liquid electrode and (c) discharge in bubbles in liquid, taken from [18].

Plasma discharges in liquids are usually ignited by high voltage pulses and a combination of pin and plate electrodes. According to Bruggeman and Leys [18], three main setups are distinguished for discharges in and in contact with liquids: Discharges directly inside liquid, gas phase discharge with liquid electrodes and discharges in bubbles in liquids, as shown in figure 1. The experimental setup used in this work corresponds to a discharge directly into liquid (see figure 1a).

To ignite plasmas inside liquids a high voltage per surface area is necessary, in order to reach high electric field strength. Therefore, either the radius of the electrode can be reduced or the voltage can be increased. The relationship between the electric field strength E and the applied voltage U is approximately

$$E \propto \frac{U}{5r_\mathrm{t}} \tag{1}$$

where r_t the radius of an electrode tip [19]. That is why most setups use sharp pin electrodes and high voltages to increase the electric field strength. To avoid an

overheating of the electrode or the liquid, short voltage pulses are utilised. The length of the pulse, especially the length of the rise time is important, as the ignition mechanism is directly depending on it.

2.1.1 Discharge Types

There are different types of discharges in liquids [2, 5, 12]. A distinction is made between corona-like, streamer-like, spark and arc discharges. Spark and arc discharges reach the opposite electrode and are only studied by a few groups [20, 21].

Corona and corona-like discharges are caused by an electrical breakdown inside the liquid due to a strong inhomogeneous electric field. Although the current flows from the electrode into the gaseous or liquid environment, the plasma does not reach the counter electrode. For positive voltage polarities, a corona-like discharge shows a homogeneous glow around the electrode tip and for negative polarities, the plasma propagates further into the environment. Streamer-like discharges arise analogously to corona-like discharges, but instead of only a homogeneous glow long filaments, the so-called streamers, with short transient lifetimes are formed. The plasma density at the streamer heads is usually higher than in the streamer channels [22].

In previous work on nanosecond discharges in water, mostly streamer-like discharge structures were observed [23–26]. According to Dobrynin et al. [27], for positive rectangular nanosecond voltage pulses with short rise times this discharge proceeds in three steps. First, plasma ignition occurs during the rising front of the pulse when a high electric field strength is reached. Then the plasma propagates through the liquid until the voltage pulse reaches its plateau. During the plateau phase, the streamer head stops and the positive charge is compensated by an electron flow. In this phase no or hardly any plasma glow is visible, which is therefore called ‘dark phase’ [24, 28]. At the falling edge of the voltage pulse, the plasma is reignited but the emission is less bright than during the initial discharge [27]. This course is congruent with the observations of Grosse et al. [23, 29].

2.1.2 Cavitation Process

Due to the pressure gradient at the electrode tip caused by the high electric field strength electrostriction occurs, which causes the molecules of the liquid to rearrange. For H_2O this means a reorganisation of the water molecules which leads to an inhomogeneous density distribution. This causes ruptures and low density regions in the water in which the plasma can ignite (more about the ignition in section 2.2). The plasma propagates in the form of streamer branches. After ignition, gas channels form in these streamer branches. The gas channels coalesce into the form of a gas bubble at the tip of the electrode. These cavitation bubbles form after the discharge for nanosecond pulsed plasmas. This is contrary to microsecond pulsed discharge (see subsection 2.2.1). The bubble is driven by a strong internal pressure at the potential energy of the bubble equals the missing water volume. This can be described by the following equation, where V_0 equals the initial volume and p_0 equals the initial pressure of the bubble

$$E_{\text{pot}} = p_0 \cdot V_0. \tag{2}$$

This potential energy is converted into kinetic energy. Therefore, the bubble expands until the pressure falls below the ambient pressure. Thereafter the bubble collapses. After collapsing, the bubble detaches from the electrode, dissipates into the liquid environment and rises to the liquid surface due to buoyancy. As outlined in Grosse et al. [29], the change of the bubble radius can be described with equation (3) simplified from the Rayleigh-Plesset equation, where h denotes the enthalpy at the bubble wall, C the speed of sound in the liquid medium and R the bubble wall radius with the velocity $\dot{R}$ and the acceleration $\ddot{R}$

$$R\ddot{R}\left(1-\frac{\dot{R}}{C}\right)+\frac{3}{2}\dot{R}^2\left(1-\frac{\dot{R}}{3C}\right)=h\left(1+\frac{\dot{R}}{C}\right). \tag{3}$$

This differential equation is just an approximation which neglects effects like condensation at the inner bubble wall. According to Vogel et al. [30], the energy, which is expanded to form the cavitation bubble, results in equation

$$E_{\text{B}} = \frac{4}{3}\pi R_{\text{max}}^3 \left(p_\infty - p_{\text{plasma}}\right) \tag{4}$$

with R_{max} being the maximal bubble wall radius, p_{plasma} the pressure of the surrounding plasma and p_ν the vapour pressure inside the bubble.

2.2 Ignition Mechanism

The ignition mechanism for pulses in the microsecond range with rise times longer than a few nanoseconds has already been sufficiently discussed and observed [2]. This mechanism corresponds to an ignition of the plasma in a previously created gas bubble. For shorter rise times below a few nanoseconds, ignition in previously formed gas bubbles is no longer possible, since the hydrodynamic response of liquids is too slow. But an ignition only due to electron collision ionisation inside the pure liquid is not possible, according to Jones and Kunhardt [15]. In the course of this section, the four currently discussed models for plasma ignition at nanosecond pulses are explained. For all this theories there is still a lack of experimental data.

2.2.1 Ignition in Gaseous Bubbles

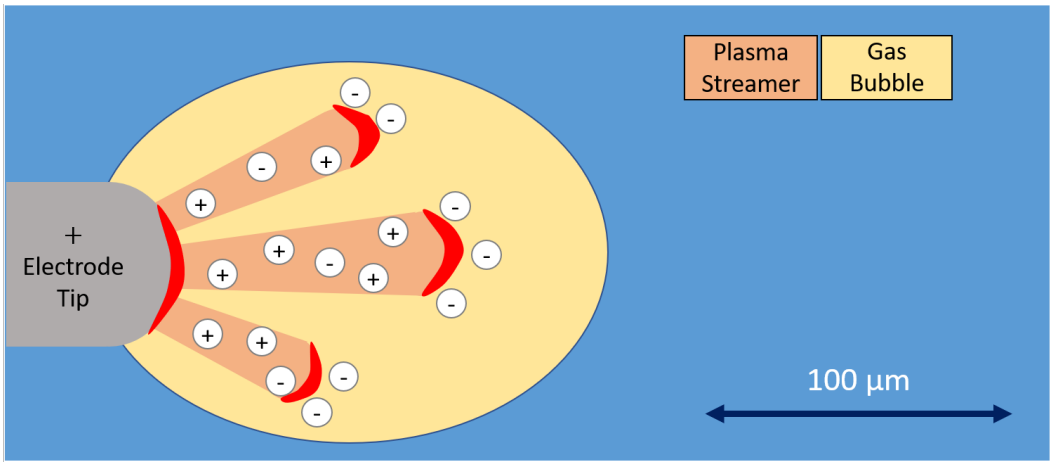

Figure 2. Sketch of plasma streamers propagating from the electrode into a previously formed gas environment inside the liquid.

Due to dissolved air in a liquid or due to evaporation, gas bubbles can occur near the electrode. Within these bubbles, electron avalanches would then ignite the plasma. However, the time required for the formation of these gas bubbles is usually in the order of microseconds [31]. Hence, voltage pulses with rising times in the order of microseconds would be necessary. If such gas bubbles were present at the time of ignition, electron avalanches inside these gas bubbles could lead to discharge ignition. In this case, the discharge would behave similarly to gaseous discharges. Therefore, positive voltage polarity would, e.g. cause a smaller electron density than pulses with negative polarity [32].

2.2.2 Nanovoids

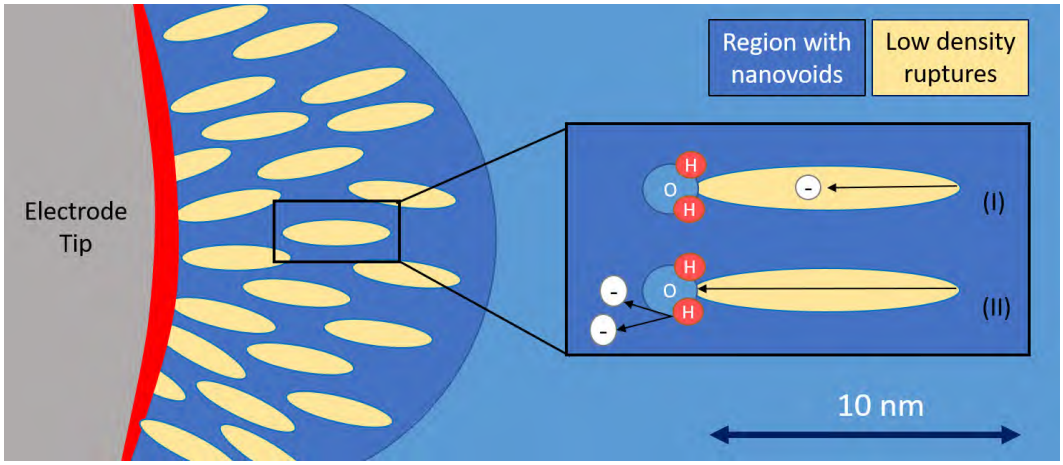

Figure 3. Sketch of the charge multiplication at the interface between nanovoids and liquid, adapted from [33].

Since the hydrodynamic reaction time of the liquid is too large for bubbles to form previous to the discharge, another mechanism must lead to discharge ignition for pulses with rising times shorter than a few nanosecond. An alternative ignition environment are the so-called nanovoids or nanopores [16, 17, 27, 31, 33–35]. These nanoscaled ruptures in the liquid occur analogously to cavitation nuclei due to high electric field strengths and the associated electrostriction. Nanovoids or nanopores, as shown in figure 3, are small ruptures or low density regions in which electrons can be accelerated by the electric field without being decelerated by the liquid. Nanopores are in the order of a few nanometres. Theoretical calculations by Aghdam et al. show, however, that a charge multiplication avalanche cannot occur on these scales [36]. Instead, individual electrons could be accelerated within these nanovoids, which subsequently would hit the interface between nanovoid and liquid. An energy transfer would take place and several electrons could be released from a molecule. In this way, a chain reaction could be initiated.

Although nanovoids are the subject of many papers, they have not yet been observed. T. Lewis [37] was one of the first to report on nanovoids. In his opinion, nanopores and field effects occur together. According to him, field effects release the free electrons and the electron multiplication is then facilitated by the nanovoids.

2.2.3 Field Effects

The work of Jones and Kunhardt [15], already mentions field emission as the trigger mechanism for plasma ignition. They proposed, that field emission heats up the liquid and thus creates regions of lower density in which the electrons can accelerate. When the density falls below a critical density of approximately $N_{\text{crit}} = 1 \times 10^{21}\,\text{cm}^{-3}$ [15], the plasma ignites and begins to propagate through the liquid. This suggests a possible combination of different models, such as the combination of nanovoids and field effects.

For different voltage polarities different field effects appear. If the applied electric field is negative, field emission occurs, so that electrons from bulk metals can tunnel into the liquid [19]. The highest energy level filled with electrons in metals is the Fermi level E_{F}, which is below the vacuum level. To generate thermal emission, the free electrons of the metal must be excited above the work function Φ.

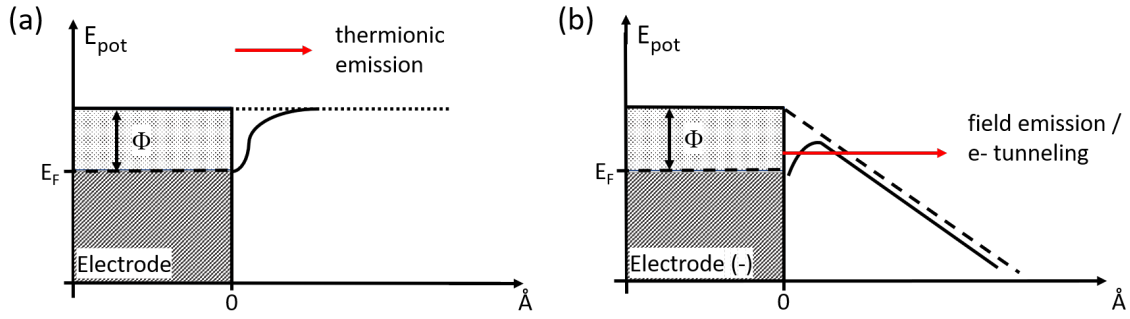

Figure 4. Thermionic emission (a) in comparison to field emission (b) at a negatively charged metal electrode. E_{F} is the Fermi level and Φ the work function of the electrode material. Adapted from [19].

However, if a negative voltage is applied to the electrode, the potential barrier deforms and the electrons can tunnel through the deformed barrier, as illustrated in figure 4. Using the simplified Fowler-Nordheim equation [38], the relationship between the current I of the tunneling electrons and the applied electric field E follows as

$$I \propto \exp\left(-\frac{4}{3}\left(\frac{2m}{\hbar^2}\right)^{1/2} \Phi^{3/2} \cdot E^{-1}\right) \tag{5}$$

where m is the effective mass, Φ is the work function and $\hbar$ is the Planck constant. The electric field must be strong enough for the potential barrier to be deformed. It is not yet known which field strength is sufficient, according to Kolb et al. $E > 10\,\text{MV/cm}$ [39] would be sufficient, according to Starikovskiy et al. $E > 30\,\text{MV/cm}$ [24] would be necessary.

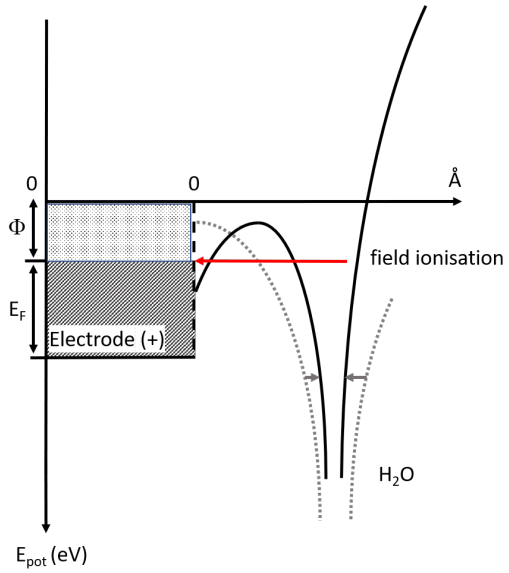

Figure 5. Sketch of the field ionisation effect, which causes electron tunneling from the H_2O molecule into the positively charged metal electrode. E_F is the Fermi level and Φ the work function of the electrode material. The dotted lines describe the undisturbed electrical potential of the molecule, which is deformed (solid line) due to the applied electric field, adapted from [19].

If a positive voltage is applied instead of a negative voltage, the direction of the electric field reverses and field ionisation occurs. During field ionisation, electrons tunnel from the liquid molecules towards the electrode. The applied positive field deforms the potential barrier of the liquid H_2O molecules. If electrons tunnel out of the potential well of the molecule and if their energy is above the Fermi level, the electrons can tunnel directly into the positively charged electrode, as shown in figure 5. Different Fermi energy levels for different materials influence the field ionisation threshold. For a tungsten tip in water, the tunneling of electrons occurs with a probability of 1-5 % above field strengths of 0.2 V/Å [19]. The effect that a high electric field strength enables electron tunneling is also called Zener effect in semiconductor technology [40].

2.2.4 Super Critical Fluids

If a fluid is put under high pressure and heated above the critical point, a super critical fluid (SCF) is created. These SCFs show both gaseous and liquid properties, especially are they dense like a liquid but have a gaseous viscosity [42]. By varying the temperature and pressure, a seamless transition from gas-like to liquid-like can be achieved. The so-called Widom line, which extends through the critical point of the liquid, divides the supercritical phase of the fluid into gaseous and liquid-like [42]. According to Simeoni et al. [43], the exact position of the fluid in the supercritical state area in

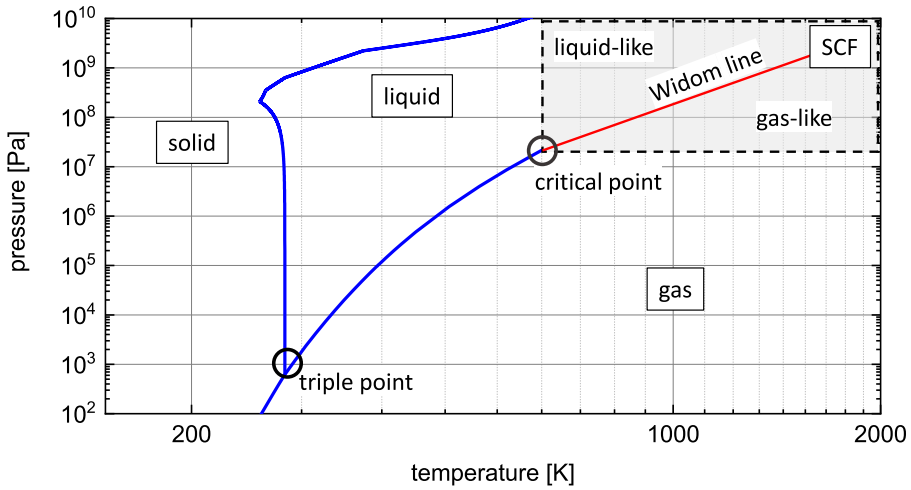

Figure 6. Section of the phase diagram of water, with the supercritical region and the Widom line (red) drawn in. Adapted from [41].

the pressure-temperature (p-T) diagram, see figure 6, has an influence on the physical properties of the fluid, including how fast acoustic waves propagate in it. This effect is also called positive dispersion.

A plasma discharge in an SCF is more likely than in a pure liquid. An SCF shows high density fluctuations on a molecular level, whereas in a liquid, the mean free path of the electrons is small [44]. For each location in the p - T diagram, these density fluctuations are different [45]. They are expressed in the SCF by a strong inhomogeneity of the molecules [46]. These form cluster-like structures, as shown in figure 7.

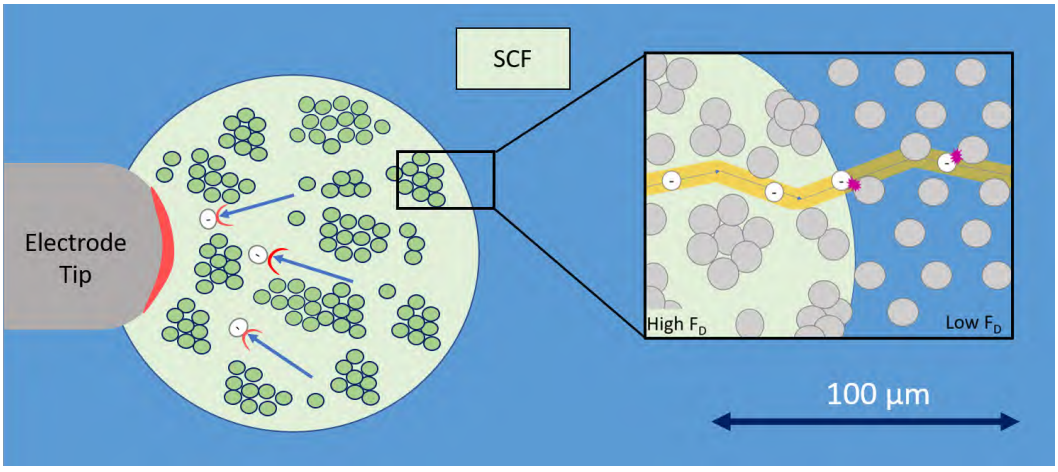

Figure 7. Sketch of the acceleration of electrons in the SCF. Adapted from [44].

It is expected that the ignition of the plasma by field effects will cause a pressure and temperature far above the critical point of water, which corresponds to a temperature of $T = 647\,\mathrm{K}$ and $p = 22.1\,\mathrm{MPa}$ [47], at the electrode tip. For nanosecond pulsed plasmas in water, pressures in the range of a few GPa [29, 48] and temperatures of several thousand K [23, 49, 50] have been observed in the initial stage of the plasma. Thus, the supercritical state of water can be reached and low density regions can be created in which electrons can be accelerated leading to plasma ignition [44]. Reaching the supercritical state would then result in a self-propagating process for the surrounding volume, since there is sufficient pressure and a high enough temperature local at the streamer head to carry further regions into the super critical state.

2.3 Emission Spectroscopy

Time-resolved optical emission spectroscopy (OES) has often been used to characterise the properties of a plasma discharge in liquids [51, 52]. OES can be used to determine not only the electron densities but can also estimate the temperature of the plasma in case of black body emitting electrodes. These accurate measurements of plasma temperatures and electron densities, are essential for understanding the formation and chemistry of in-liquid plasmas. In this section, first the continuum spectrum is explained followed by the characteristic spectral lines in connection with the occurring broadening effects.

2.3.1 Continuum Spectrum

The continuum spectrum has several origins, which are described in detail in [41]. It is discussed that continuum emission from free-free and free-bound radiation is most likely to form continuum radiation during the initial phase of nanosecond pulsed plasmas in liquids [53]. However, recent measurements show that black body radiation from the electrode tip could contribute highly to the continuum emission [41, 50]. This difference can be explained by the dependence on the applied voltages in combination with the size of the electrode tips. In their work, Simek et al. [54] have used larger electrodes, which heat up less due to their larger surface area. For this reason, the proportion of black body radiation in their work can be lower than in this work. The continuum radiation emitted by the hot metal electrode can be described by black body radiation, for which Planck's law applies

$$\epsilon(\lambda, T) = \frac{2hc^2}{\lambda^5} \frac{1}{\exp\left(\frac{hc}{\lambda k_\mathrm{B} T}\right) - 1} \tag{6}$$

where ϵ is the spectral radiance, h is the Planck's constant, c the speed of light, k_B the Boltzmann constant, λ the wavelength and T the temperature.

2.3.2 Spectral Lines

Every atom emits energy in the form of electromagnetic radiation during relaxation after excitation. These emission lines are characteristic for each element and can be detected with OES. Spectral lines can be influenced by certain physical processes leading for example to a broadening of the lines [55]. The broadening effects include pressure broadening, Doppler broadening, opacity broadening and instrumental broadening due to the experimental setup. These mechanisms are explained in depth in K. Grosse [41]. In the context of this work, only pressure broadening, especially Stark broadening, and opacity broadening will be discussed.

Pressure broadening reflects the influence of surrounding particles on the spectral line. Stark broadening occurs due to the splitting of the energy levels in an electric field and can provide information about the electron density. The splitting of the energy levels is caused by the interaction of electrons with the dipole moment of the external electric field [55].

Opacity broadening depends on the optical depth τ of the plasma. The thicker the optical depth of a plasma, the more particles are absorbed along the optical path. The absorption of photons leads to a self-reversal of an emission line. Since the reabsorption probability in the center is higher than in the wings of the line, an intensity drop can be generated without affecting the full width half maximum (FWHM) [55].

3 Experimental Setup and Methods

In order to gain a better understanding of the effects that lead to non-thermal plasma ignition directly in a liquid, a set-up consisting of two opposing pin electrodes in distilled water is examined in this work. In particular the set-up of plasma and shadow photography as well as optical emission spectroscopy (OES) and scanning electron microscopy (SEM) is considered.

3.1 In-Liquid Setup

The experimental setup for igniting the in-liquid plasma is described in this section. It consists of a plasma chamber and two nanosecond pulsers, each of which can generate a 15 ns pulse with different polarity. The back current shunt, short BCS, used to measure the voltage pulse is also explained.

3.1.1 Plasma Chamber

Figure 8 shows the structure of the plasma chamber. It is made of polymethyl methacrylate (PMMA) and contains approximately 25 ml of distilled deionised water. A pin-to-pin electrode assembly is implemented in the chamber consisting of two copper rods mounted in glass tubes, in which stainless steel cannulas are inserted. For the powered electrode an additional 50 µm thin metal wire is clamped into the cannula, to enhance the electric field at the electrode tip. In this work, electrodes made of tungsten (W), platinum (Pt) and platinum iridium alloy (Pt/Ir) wire are used. The electrodes have an approximate electrode spacing of 1 cm. While the lower electrode is grounded, the electrical pulse is applied to the upper electrode. The used wires are analysed before and after plasma ignition with the SEM described in subsection 3.2.4. The used tungsten electrodes are visible as a close-up in figure 22.

The plasma chamber has four in- and outlets for liquid with closable valves. In addition to filling and draining the liquid, this also allows operation in a flow mode with water flow controlled by a pump. In the context of this work, only distilled water is considered as liquid in a steady-state mode, without a liquid flow during the discharge treatment. In addition to the inlets and outlets for the electrodes, the chamber has three fused silica UV broadband windows for optical measurements of the plasma. Two are located in the line-of-sight of the plasma on the sides of the chamber, as can be seen in figure 8. These are used for imaging diagnostics as plasma photography and shadowgraphy. The large window at the front of the chamber is used for OES, which is described in subsection 3.2.3.

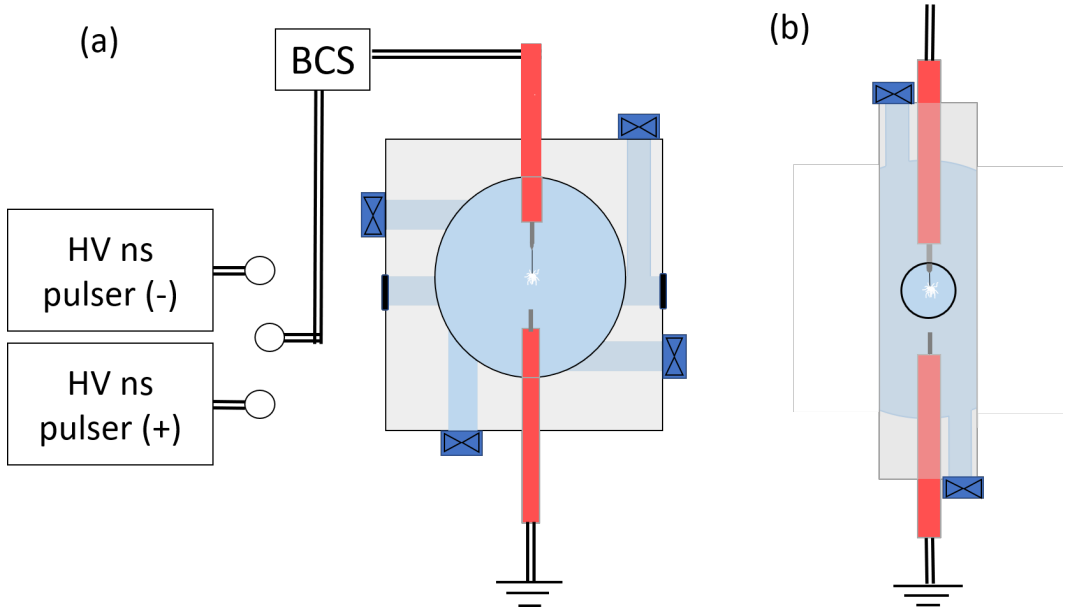

Figure 8. Setup of the plasma chamber in (a) front view with 10 m long cable connection to the nanosecond high voltage pulsers and (b) side view.

3.1.2 Nanosecond Pulsed High Voltage Generators

The voltage sources of the experimental setup for igniting the plasma are high voltage pulser from FID Technology GmbH. There is one pulser for each polarity. The positive pulser is the FPG 30-01NK10, which is capable of generating 10 ns pulses with rise times of 2 - 3 ns. The voltage amplitude can be changed from 10 - 30 kV, the frequency from 1 - 100 Hz and the trigger from internal to external. The negative pulses are generated by FPG 30-01NK10-NEG and can be changed identically to the positive pulses in frequency, voltage and trigger setting. As shown in figure 8, the pulsers can be alternately connected to the electrode via a 10 m long RG217 coaxial cable with a BCS mounted in the middle of the cable for voltage measurements. In this work, a cable with a length of 10 m is used to delay reflections in the BCS signal, which are created at the electrodes due to a mismatch in impedance. This reflected pulse can arrive at the electrode again and thus influence the plasma. The so caused disturbance can be delayed by selecting a longer cable length. With a cable length of 10 m, these reflections appear after 100 ns and do not influence the first main plasma emission and cavitation.

The entire setup is endosed by a Faraday cage and incoming and outgoing cables are covered by ferrite cores. This is necessary because due to the high voltage pulses with very short rise times, high electromagnetic interference occurs, which otherwise affects the surrounding electronic devices.

3.2 Diagnostics and Methods

3.2.1 Electrical Measurements

To calculate the shape of the electrical voltage pulse and the dissipated energy, a BCS is used in combination with an HD6104A oscilloscope from Teledyne LeCroy GmbH. The BCS consists of eleven $R = 3.3\,\Omega$ resistors connected in parallel, which are inserted in the return conductor of the coaxial cable. The total resistance is therefore $R_{\text{shunt}} = 0.3\Omega$. The high current flow during the HV pulse induces a current signal in the BCS, which can then be measured with the oscilloscope. This measurement technique is described in more detail in K. Grosse [41]. Overall, the relation between the voltage pulse $U(x,t)$, the cable resistance R_{coax} and the current flowing in the cable is $I(x,t)$ is as follows

$$U(x,t) = R_{\text{coax}} \cdot I(x,t) = 105.1 \cdot R_{\text{coax}} \cdot U_{\text{osci}}, \tag{7}$$

with the voltage U_{osci} determined from attenuators which prevent the oscilloscope from damage. By measuring with the BCS, the shape of the voltage pulses can be traced. The voltage pulse shape is correlated to the temporal evolution of the plasma intensity. An overview of the determined shape of the pulse can be found in figure 9 for both polarities.

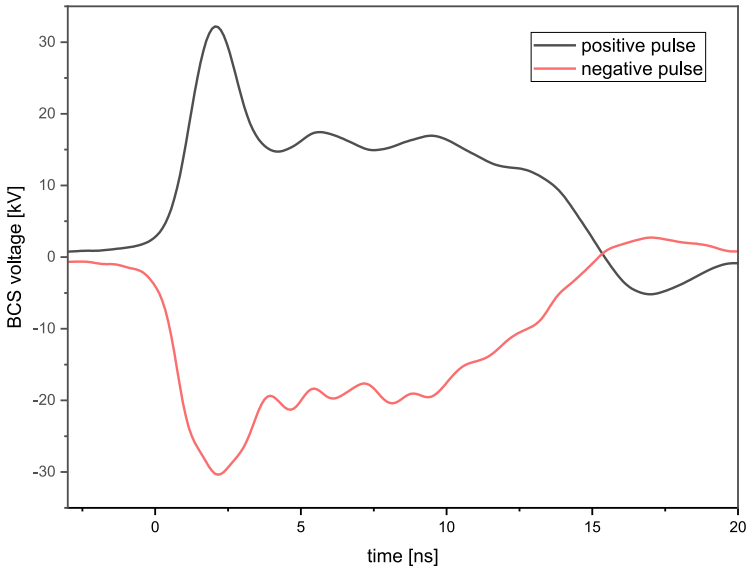

Figure 9. The measured voltage pulse generated by the positive polarity pulser (black) and the negative polarity pulser (red).

3.2.2 ICCD Imaging

Phase-resolved intensified charge-coupled device (ICCD) imaging is used to determine the optical appearance of the plasma emission and its intensity distribution over time. By means of a lens, the emitted light can be directed onto the CCD chip of an Andor iStar camera.

The Andor iStar camera is synchronised with the pulse generator via its external trigger output. Due to cable and internal delays, the camera is set to a delay time of 439±2 ns for the negative pulse and 486±2 ns for the positive pulse after the initial trigger signal. This delay is arbitrary and chosen so that a first emission starts with the rise of the voltage pulse. The plateau of the pulse is then responsible for the 'dark phase', a non-luminous phase of plasma ignition. This is consistent with the findings of Starikovski et al. [24] and Dobrynin et al. [27]. These steps in plasma development have also been observed in the past with the same experimental setup as used in this work [23, 29, 50]. Due to the limited speed of the camera each image is taken for another pulse with a time delay of 2 ns to display an entire pulse and thus to gain information about the emission intensity, the position of the plasma in relation to the electrode and the behaviour of the discharge.

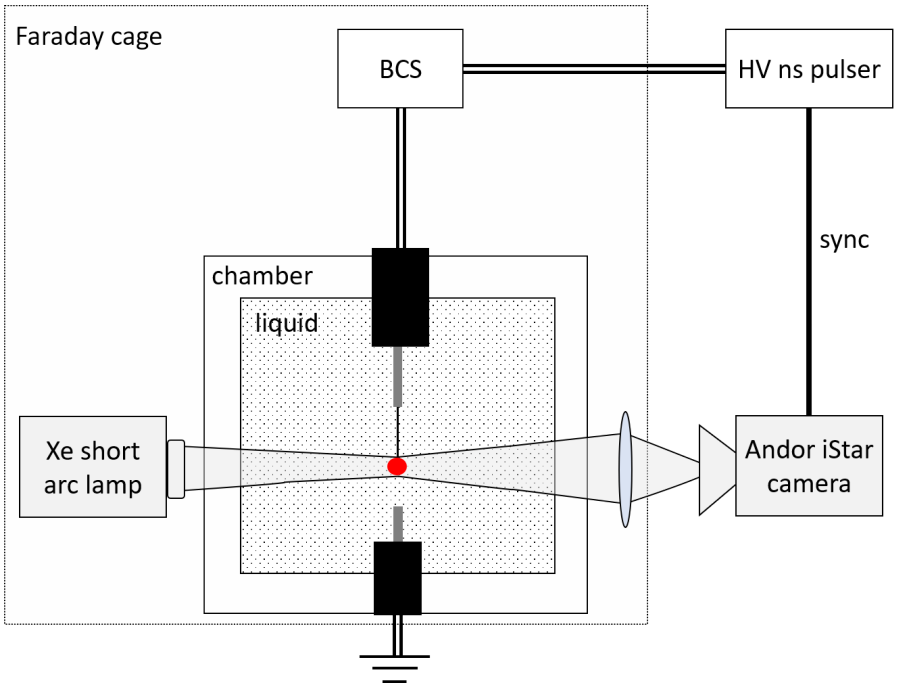

Figure 10. Sketch of the measurement setup for shadowgraphy. The Andor iStar camera, synchronised with the pulser, records the light from the Xenon lamp or the light emission from the plasma, focused through a lens. Adapted from [50].

The setup used for shadowgraphy is similar to the setup for plasma photography, except for the addition of a Xenon arc lamp, as shown in figure 10. The light beam illuminates the electrode tip through the windows of the plasma chamber. Due to the differences in the refractive index of the liquid and the plasma, density gradients as e.g. for acoustic waves and the changing structure of the cavitation bubble after the plasma discharge can be made visible.

3.2.3 Optical Emission Spectroscopy

OES is used to draw conclusions about the composition of the plasma, such as the excited species, via their spectral line emission. The change in the emission spectrum over time is observed. Broadening effects, such as Stark broadening, can be used to draw conclusions about the electron density and the analysis of the continuum radiation as black body radiation yields inferences about the temperature of the electrode.

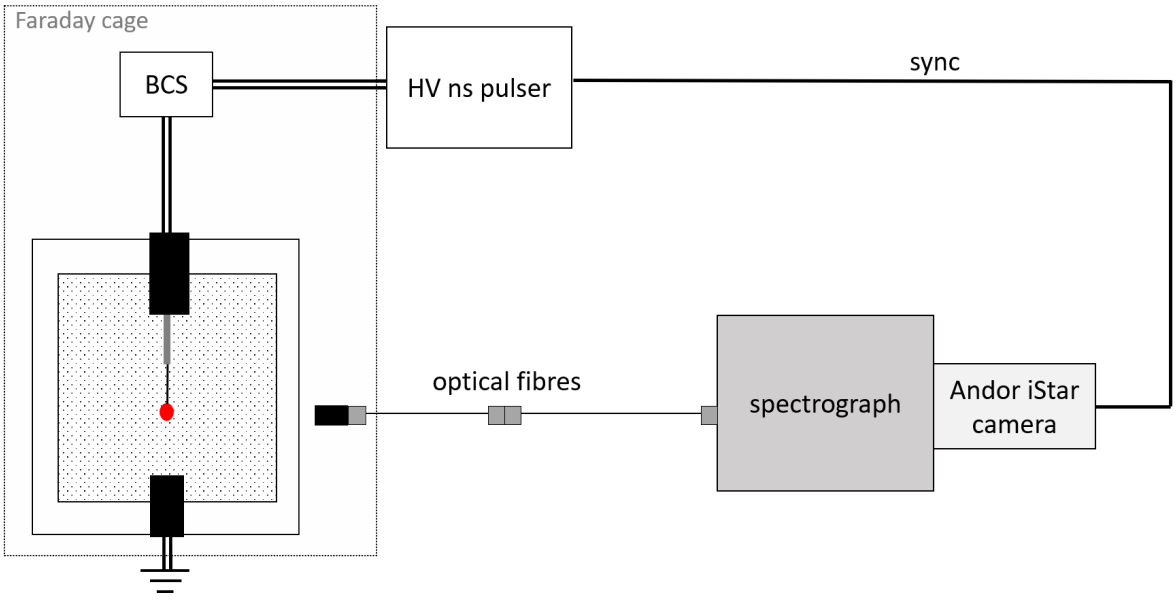

Figure 11. Sketch of the optical emission spectroscopy with the plasma chamber inside a faraday cage. The emitted light was collected by a collimator connected to the SpectraPro 750 spectrograph via optical fibres. The used camera types were synchronised with the high voltage pulser. Adapted from [50].

The structure of the OES setup is outlined in figure 11. A triple-grating Spectra Pro 750 spectograph from Acton Research was used in combination with the Andor iStar camera, which was also used for the ICCD photography. Here a gate time of 2 ns and time steps of 2 ns between the individual spectra measurements were used. The grating used is 50 $\frac{\text{grooves}}{\text{mm}}$ blazed at 600 nm. Each spectrum was averaged over 2000 plasma pulses.

Since the CCD chip has only a limited size, the spectrum was split into three parts with different central wavelengths. These are 400 nm, 550 nm and 850 nm. Because the second order reflections become visible at wavelengths above 500 nm, these are filtered out with a cut off filter. For this purpose, the emission spectra measured with a central wavelength of 550 nm are measured both with and without the cut off filter. The spectrum with the central wavelength at 400 nm is measured without the cut off filter and the spectrum from 850 nm is only measured with the cut off filter.

The spectra were calibrated with a broadband D-halogen lamp and the background was subtracted. Since the camera has an instrumental profile of 2.3 nm, this was measured with a helium neon laser and included in the calibration. Subsequently, the individual OES measurements were merged with a Matlab program.

3.2.4 Scanning Electron Microscopy

To be able to determine possible surface changes on the electrode, the electrodes were observed before and after treatment with plasma using an environmental scanning electron microscope (ESEM). This works analog to a SEM, where the sample is scanned by an electron beam and an image is generated by detecting the back radiation due to the interacting effect of the sample with the electron beam. The difference is the gas pressure in the sample chamber. While an SEM works with high vacuum in the sample chamber, the ESEM is able to operate at a pressure of 1300 Pa [56].

Two electrode tips of each material were imaged at 1000x, 3000x, 6000x and 8000x magnification before and after plasma ignition. The tips were used to ignite the plasma for 25 to 30 minutes, one per material with a positive voltage pulse and one with a negative voltage pulse. The images taken are shown in figures 22 - 24.

4 Results

In the following chapter, the results of the measurements are analysed and discussed to compare them with the ignition models presented in the theoretical background section 2.2. The aim is to work towards a verification or falsification of the individual theories describing discharge ignition inside a liquid. Difficulties encountered during the measurement process are discussed along with their possible solutions.

4.1 Plasma Dynamic

A large component of this work and an important aspect for deriving the ignition mechanism is the analysis of the appearance and propagation of the plasma. In this section, special attention is paid to the visible light emission and its development over time. This development of the light intensity over time is placed in the context of the time evolution of the voltage pulse. The dissipated energy can by determined by comparing the initial and reflected power pulse over time taken from the BCS signals. In addition, the shape of the pulse at the electrode tip is reconstructed by composing the initial and reflected pulse. Initially, the visual and energetic differences for both polarities are compared to each other; afterwards the different materials are dealt with in section 4.4.

4.1.1 Electrical Characteristics

Figure 12 shows the BCS voltage over time oscillating between electrode tip and ns pulser. The initial pulses are visible from 0 - 15 ns, followed by the reflected pulses at the electrode (grey marked area from 45 - 70 ns). The third pulse shows the reflection at the pulser, travelling back towards the electrode, which causes a reignition of the plasma after $t = 100\,\text{ns}$. As can be seen, reflected pulses for the two polarities only differ in shape after the reignition of the plasma.

The energy dissipated in the discharge can be determined from the difference between the initial and reflected pulses. This results in $E_+ = 18\,\text{mJ}$ for the discharge with the positive polarity and is lower for the negative polarity with $E_- = 12\,\text{mJ}$. These different energies could indicate an ignition mechanism that works differently for positive pulses than for negative pulses. For example, the differences in dissipated energy could originate from the different energy thresholds necessary for field emission and field ionisation. During field emission, the first electrons can escape the electrode tip after overcoming the threshold, whereas for field ionisation, more energy is needed to reach the higher ionisation threshold.

The energy required to create nanovoids or SCF is polarity independent. However, the difference in energy is small ($\Delta E = 6\,\mathrm{mJ}$), it can possibly be within the systematic error, since the measurement method has only a limited accuracy. A precise modelling of the voltage pulse within the electrode tip would be useful to verify the observation described above and to consider the energy difference in a more detailed manner. However, it was not possible to determine the exact shape of the pulse inside the electrode within the scope of this work. Only a rough estimation of the electrode voltage is made by adding the initial and reflected pulse simulating the overlap at the point of reflection.

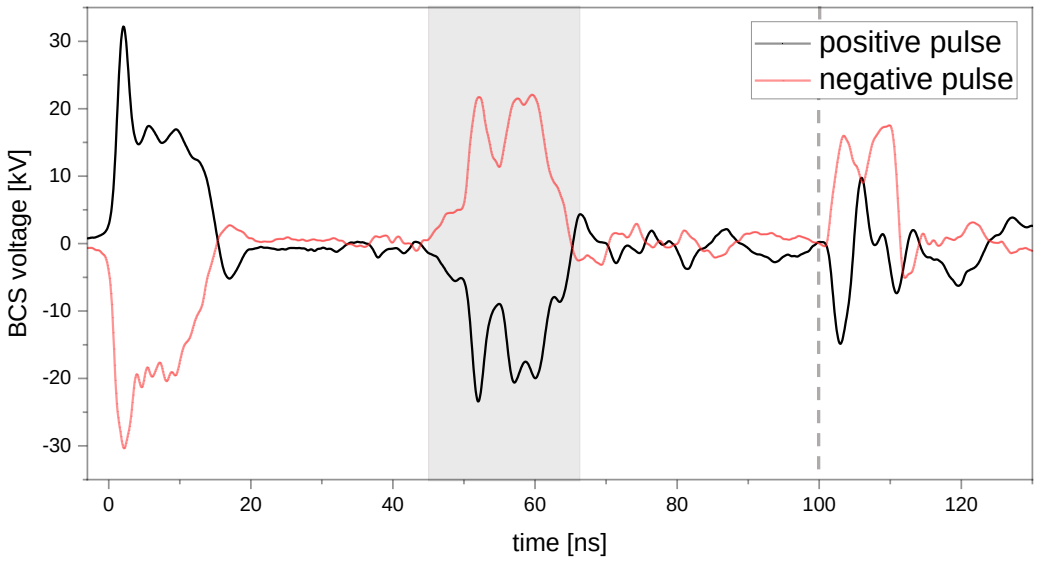

Figure 12. Development of the measured voltage pulses over time. The grey shaded area corresponds to the reflected pulse on the way back to the pulser. After 2 reflections, this pulse leads to a second ignition of the plasma after about 100 ns (grey dashed line).

4.1.2 Imaging of Plasma

In figure 13 the time evolution of the visible discharge emission at $\pm 20\,\mathrm{kV}$ recorded with the ICCD camera is shown. The images are showing the emission at the W electrode tip (white lines) in distilled water. Each image is shifted in time by 2 ns so that the whole plasma pulse is monitored. The images were taken in single shot mode and have not been accumulated. Clearly recognisable in all images are the bright regions directly at the electrode as well as the streamers extending in all directions. It is striking that the several bright locations directly at the electrode are not just a single corona-shaped region. It can therefore be assumed that these are streamer-like discharges.

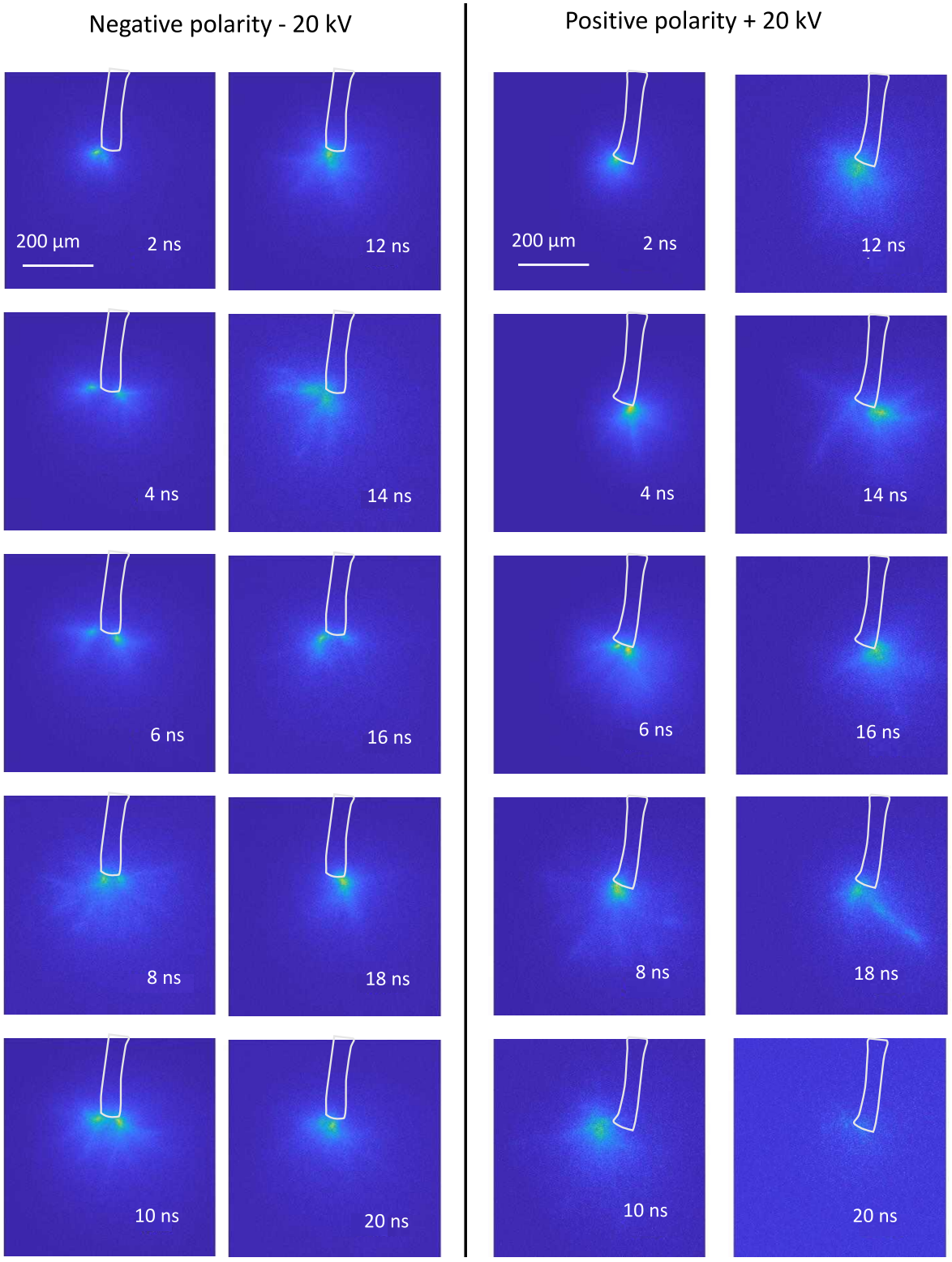

Figure 13. ICCD images of plasma emission for negative polarity (left) and positive polarity (right). The position of the W electrode is reproduced by means of white lines and the time stamp for each image is in the right-hand corner. The size scale is illustrated in the top left image.

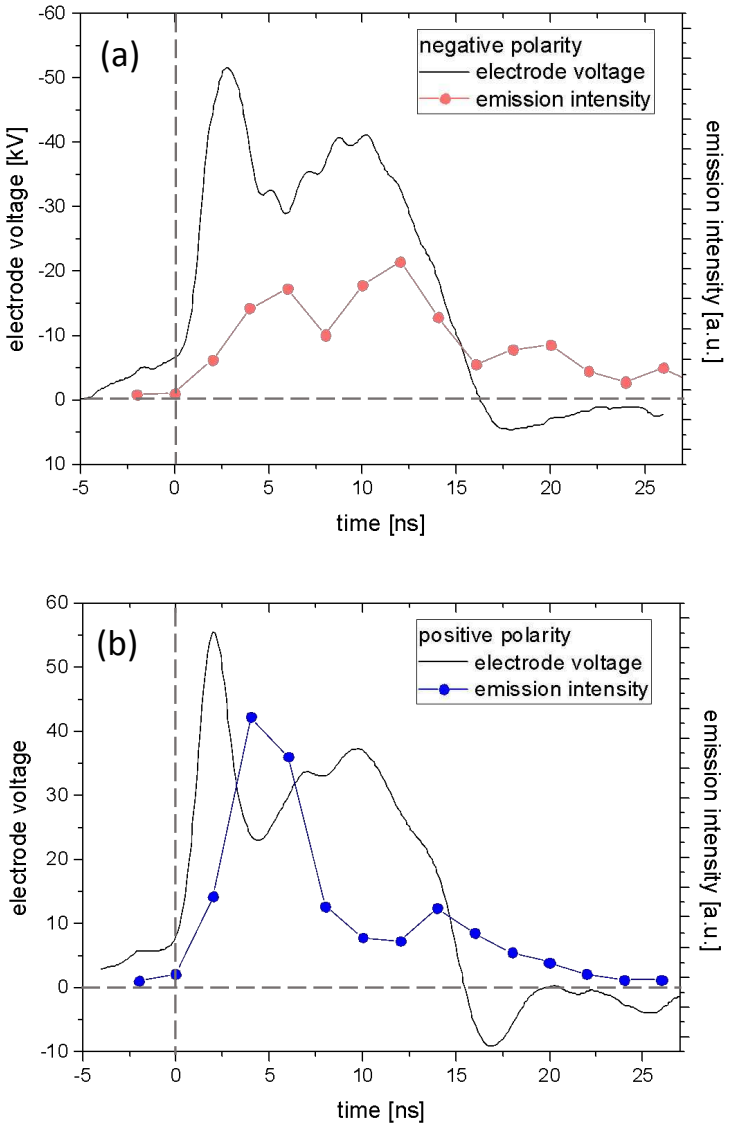

Figure 14. Integrated light intensity for the negative (a) and the positive (b) pulse polarity against time in comparison to the reconstructed voltage pulse (black). The graphs correspond to the measurements shown in 13. The dotted lines denote $t = 0\,\text{ns}$ and $U = 0\,\text{kV}$ and the y-axis are scaled equally for both graphs.

The temporal development of the discharge seems to be the same for both polarities, with a few exceptions. For both polarities, the highest light intensity is reached 4 ns after ignition, which can be seen more clearly in figure 14. While the emission intensity around the electrodes reaches its minimum at 8 ns, the streamers seem particularly bright here for both polarities. Then, the intensity around the electrode is rising again until hardly any emissions can be seen at 20 ns for the positive polarity. The plasma ignited with negative pulse polarity seems to show emission over a longer time compared with the positive pulse polarity. During the entire discharge, the brightest locations are always in the immediate vicinity of the electrode surface, while the streamers and their heads shine less intensely.

A measurement of the voltage pulse shape using a voltage probe is not possible due to the high electromagnetic radiation, which is why the measurement is made indirectly via the BCS. The shape of the voltage pulse at the electrode tip is therefore generated by the additive superposition of the first pulse and the reflected pulse. However, the simultaneous measurement of the voltage pulse and the plasma emission is not possible due to the high electromagnetic radiation, which is why the voltage pulse and the intensity curve must be manually adjusted to each other in terms of time. The rise time of the voltage pulse leads to a first plasma ignition, which can be delayed by a time of up to 2 ns. As in Dobrynin et al. [27], a dark phase follows during the plateau of the voltage pulse, which is followed by a renewed intensity peak matching the falling voltage edge.

Since two different generators have been used to generate the voltage pulse, minimal differences in the shapes of the voltage pulses occur. Those differences are small compared to the voltage amplitudes so that they can be neglected. It is noticeable in figure 14 that the temporal development of the emission intensity differs for different voltage polarity. Both polarities provide a maximum intensity at 4 ns. For the positive polarity, this maximum at the rising edge of the voltage pulse is the brightest peak of the discharge. The intensity maximum at the falling edge is significantly lower. For the negative voltage, there are two maxima within the voltage pulse. One at the rising edge and one in between the pulse at around 12 ns, maybe caused by the little rising edge of the voltage pulse around 6 - 13 ns, due to the reflection of the voltage pulse in the electrode. These maxima are approximately equally strong, although significantly weaker than the first maximum of the positive polarity. The minimum in the dark phase is weaker and longer for the positive pulse than for the negative pulse.

These observations suggest a polarity dependence of the ignition of the plasma. This can be explained with the theory of field effects, because different pulse polarities lead to different field effects. While field ionisation occurs for positive voltage pulses, field emission takes part for negative polarities. Once the plasma is ignited it propagates through a low pressure medium. The propagation looks similar for both polarities which supports a combined theory of field effects for the creation of the first free electrons and a multiplication of these within nanopores or inside supercritical water region.

While the plasma of the positive pulse does not ignite again after the second maximum at approximately 15 ns, many smaller maxima are recognisable for the negative voltage pulse, which behave equivalently to the fluctuations of the voltage pulse. This observation could imply an ignition due to field effects, since field emission takes place at the negative electrode which could be triggered by the smaller voltage fluctuations.

For field ionisation at the positive electrode, the voltage fluctuations are too small to trigger electrons from the surrounding H_2O molecules. With the rising edge of the first pulse, the molecules closest to the electrode are ionised and the plasma can spread. The molecules that could be ionised with further rising edges of the pulse are located behind the created plasma. However, since the field strength decreases with distance, the field strength at the H_2O molecules would no longer be sufficient to ionise these. To cause a reignition for field ionisation would therefore require a higher voltage or a region of new molecules that have not yet been ionised located near the electrode.

4.2 Bubble Cavitation

The cavitation bubble is created and expands due to the high initial pressure during plasma ignition, as described in subsection 2.2.1. The bubble size was determined from the shadowgraphs in appendix A.2 and the radius was measured from the electrode tip towards three points in different directions at the interface between gas bubble and water. This made it possible to determine the mean value and the accuracy of the measurement. In the shadowgraphs, expanding gas channels around the bubble are visible, these are formed in the area of previous plasma streamers. Due to their randomness and irregularity, they are not taken into account for the calculation of the gas volume.

However, the rough observation is sufficient to apply the Rayleigh-Plesset model, equation (3), and to calculate the dissipated energy. The results for the bubble radius evolution from the shadowgraphs and the resulting model for $\pm 20\,\mathrm{kV}$ is shown in figure 15. As in Grosse et al. [29], an ambient pressure of $p_{\mathrm{ambient}} = 1 \times 10^5\,\mathrm{Pa}$ and an initial bubble radius of $R_0 = 25 \times 10^{-6}\,\mathrm{m}$, which corresponds to the radius of the electrode, were used. The initial pressure is thus $p_{0,\mathrm{gas}} = 1.5 \times 10^8\,\mathrm{Pa}$ for the positive polarity and $p_{0,\mathrm{gas}} = 2 \times 10^8\,\mathrm{Pa}$ for the negative.

Although these modelled initial pressures show slight differences in the bubble radii, these differences occur mainly in the first $5\,\mu\mathrm{s}$ and last $50\,\mu\mathrm{s}$. This can be explained by the fact that in the initial phase of bubble cavitation, a particularly large number of outgoing gas channels occur at the positions of the previous streamers. These could not be taken into account in the evaluation due to their irregularity. In the final phase of bubble evolution, the bubble collapse, the model also deviates from the measurement

results, which decrease more slowly than expected. This is due to the simplicity of the model, which does not take into account adhesion to a solid surface, as it happens in reality due to the W electrode in the middle of the cavitation bubble. In principle, the modelled values fit the development of the measured radii sufficiently well.

The initial pressure multiplied by the area of the resulting bubble gives a volume energy of $E_{\mathrm{vol},-} = 1 \times 10^{-5}\,\mathrm{J}$ for the negative and $E_{\mathrm{vol},+} = 1.3 \times 10^{-5}\,\mathrm{J}$ for the positive pulse. This energy is significantly lower than the dissipated energy, which was calculated from the BCS measurement $E_{\mathrm{inital}} \approx 1$ - $2 \times 10^{-2}\,\mathrm{J}$ for both polarities. This is reasonable because not all the dissipated energy flows into the expansion of cavitation bubbles, but effects such as photon emission, heating of the electrode surface and dissociation consume energy.

The cavitation model shows that the dissipated energy, which drives the cavitation expansion and the resulting bubble radius differs only minimally for the different polarities. The difference in radius is significantly larger when the voltage is varied, see Grosse et al. [29]. Therefore it is assumed that the plasma propagation does not depend on the polarity of the voltage pulse, which is congruent to the observed plasma evolution in subsection 4.1.2. The similarity in the evolution and propagation of plasma in streamers for both polarities, implies that the gas channels formed from these streamer branches are also similar. These gas channels contain the hot gas, which contracts during the bubble development to form the bubble at the electrode tip. A main reason for the approximately same size of the bubbles for different polarities is probably the energy which dissipates into the plasma. The observation of the nearly same bubble radii therefore strengthens the theory that approximately the same amount of energy is dissipated in the plasmas for both polarities.

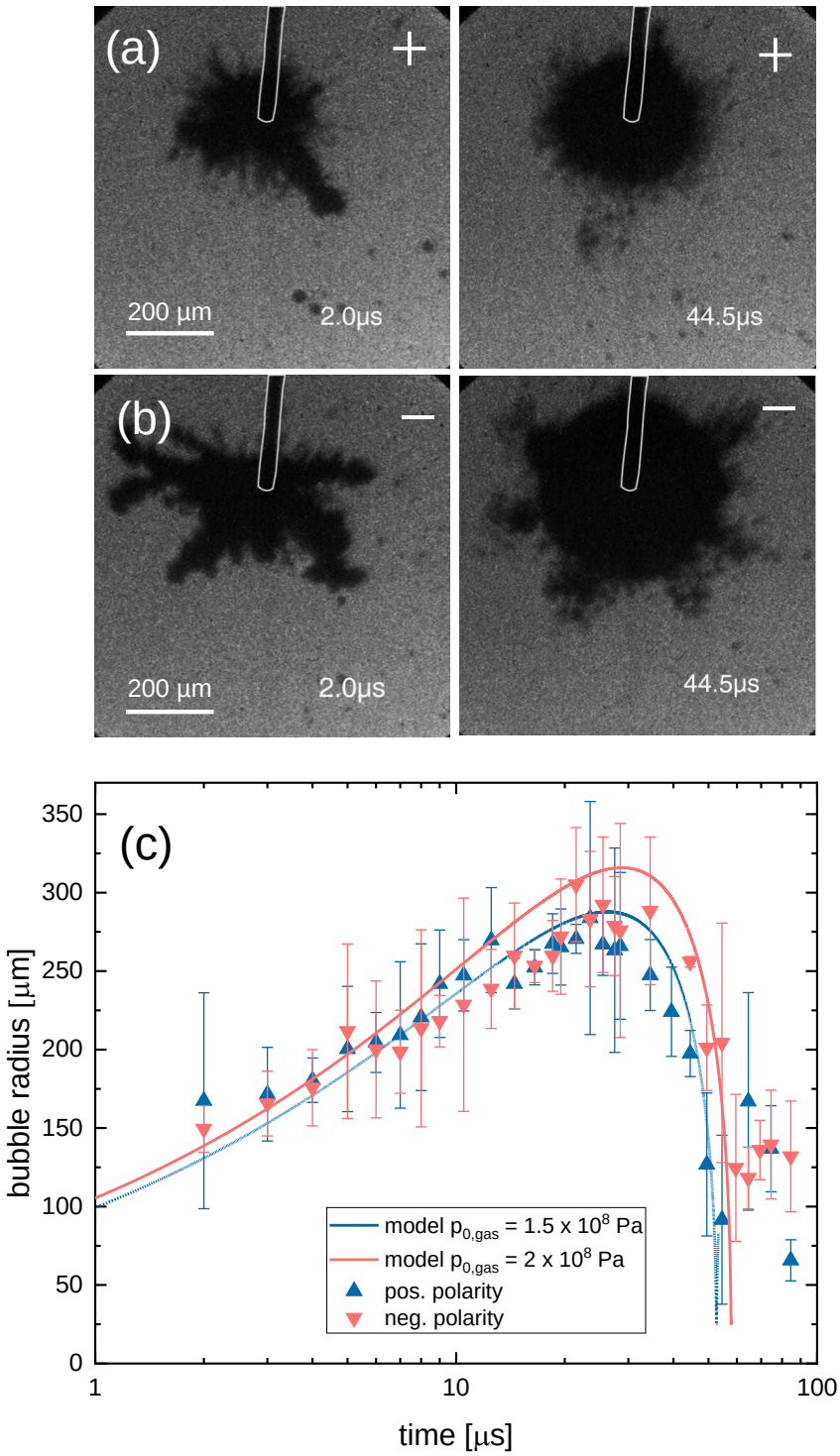

Figure 15. Shadowgraphy images of the bubble formation at different times after the plasma ignition for the positive (a) and negative (b) polarity and $U = 20\,\mathrm{kV}$. The position of the W electrode is marked in white. Time development of the bubble radii (c) for the negative (red triangle) and the positive (blue triangle) polarity. The solid lines illustrate the radius evolution due to the Rayleigh-Plesset modelling with an initial pressure of $p_{0,\mathrm{gas}} = 2 \times 10^8\,\mathrm{Pa}$ for the negative and $p_{0,\mathrm{gas}} = 1.5 \times 10^8\,\mathrm{Pa}$ for the positive pulse.

4.3 Optical Emission Spectroscopy

The recorded spectra for $\pm 20\,\mathrm{kV}$ and $\pm 16\,\mathrm{kV}$ are presented in waterfall plots in appendix A.3 to show a clear intensity and continuum radiation evolution. In figures 17 and 16 the spectra are stacked to show the evolution of the emission lines over time more clearly. The recorded spectrum for $+16\,\mathrm{kV}$ with the central wavelength of $\lambda = 400\,\mathrm{nm}$ was disturbed (probably by electrical noise) so that some of the spectra cannot be analysed. Therefore, both 16 kV spectra are starting with the measurement at a central wavelength of 550 nm. These measurements are still valuable since the most important emission lines are included. Additionally, the $\pm 16\,\mathrm{kV}$ spectra are less intense then the $\pm 20\,\mathrm{kV}$ spectra, which is why the poor signal-to-noise ratio above $\lambda > 750\,\mathrm{nm}$ has a more significant effect and only the spectra up to 750 nm were displayed for $\pm 16\,\mathrm{kV}$ and used for the modelling.

In figures 16 and 17 is recognisable that the positive spectra exhibit a higher intensity continuum radiation between 6 - 10 ns compared to the negative spectra for both applied voltage amplitudes. While the hydrogen Balmer lines can be clearly identified for the higher applied voltage, the continuum radiation predominates in the spectra with lower voltage. Nevertheless, in all four spectra ($\pm 20\,\mathrm{kV}, \pm 16\,\mathrm{kV}$) the strongly broadened H_α line can be identified at 656 nm.

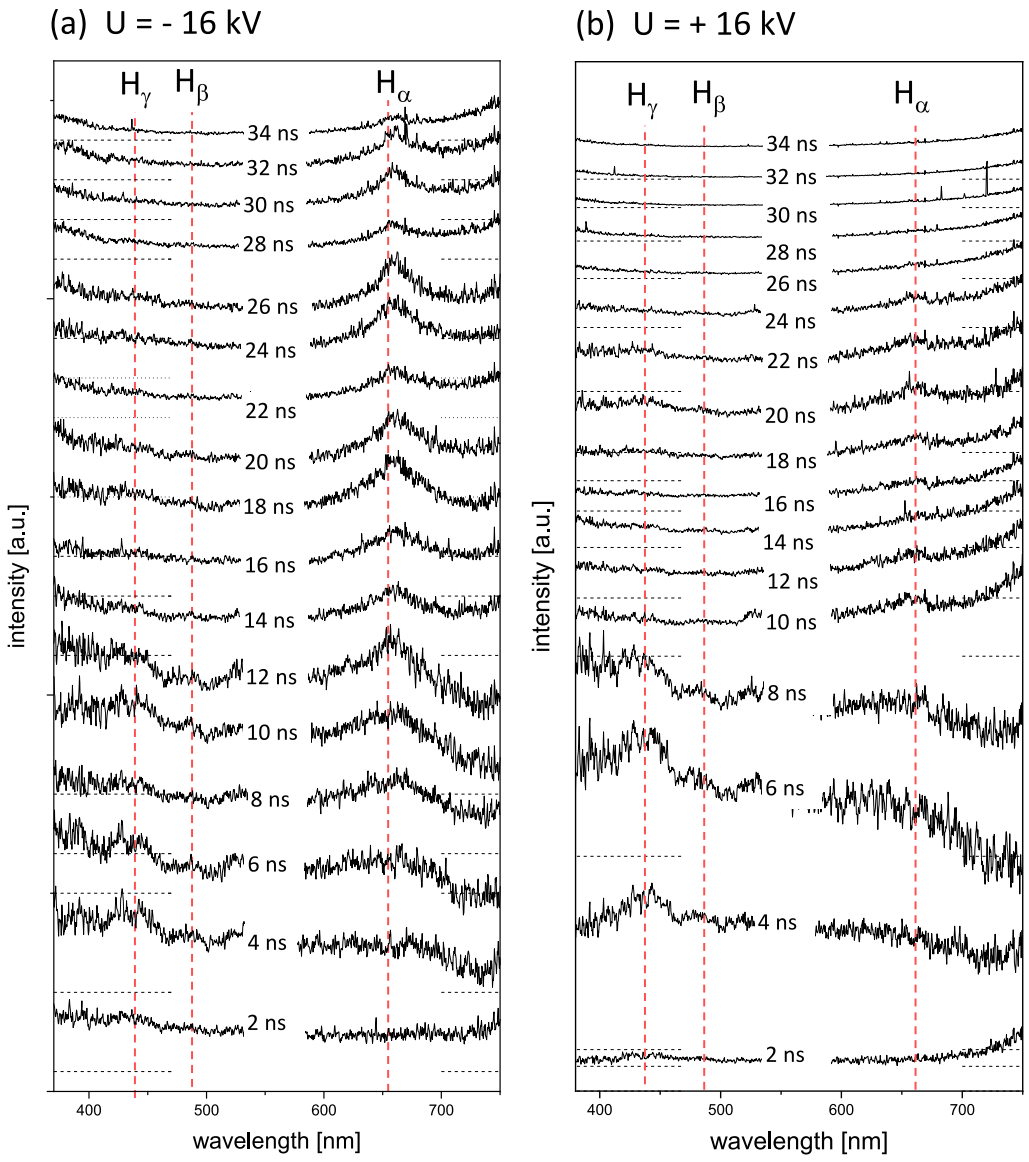

Figure 16. Temporal evolution of optical plasma emission for negative (a) and positive (b) polarity at $U = 16\,\mathrm{kV}$. The offset stacking is chosen for better visibility of the broadened emission lines H_α, H_β and H_γ (red lines).

The analysis of the spectra is performed in two main steps, as described in [29, 50]. First, the continuum radiation is determined, for which the positive polarities consists mainly of black body radiation, as shown in appendix A.3 in figure 31 for one time step at $t = 4\,\mathrm{ns}$. The strong black body radiation is caused by the high temperature at the electrode surface. At 4 ns where the plasma intensity reaches its maximum, the black body temperatures from the model are $T_{20,+} = 7000\,\mathrm{K}$ for 20 kV and $T_{16,+} = 6000\,\mathrm{K}$ for 16 kV, respectively.

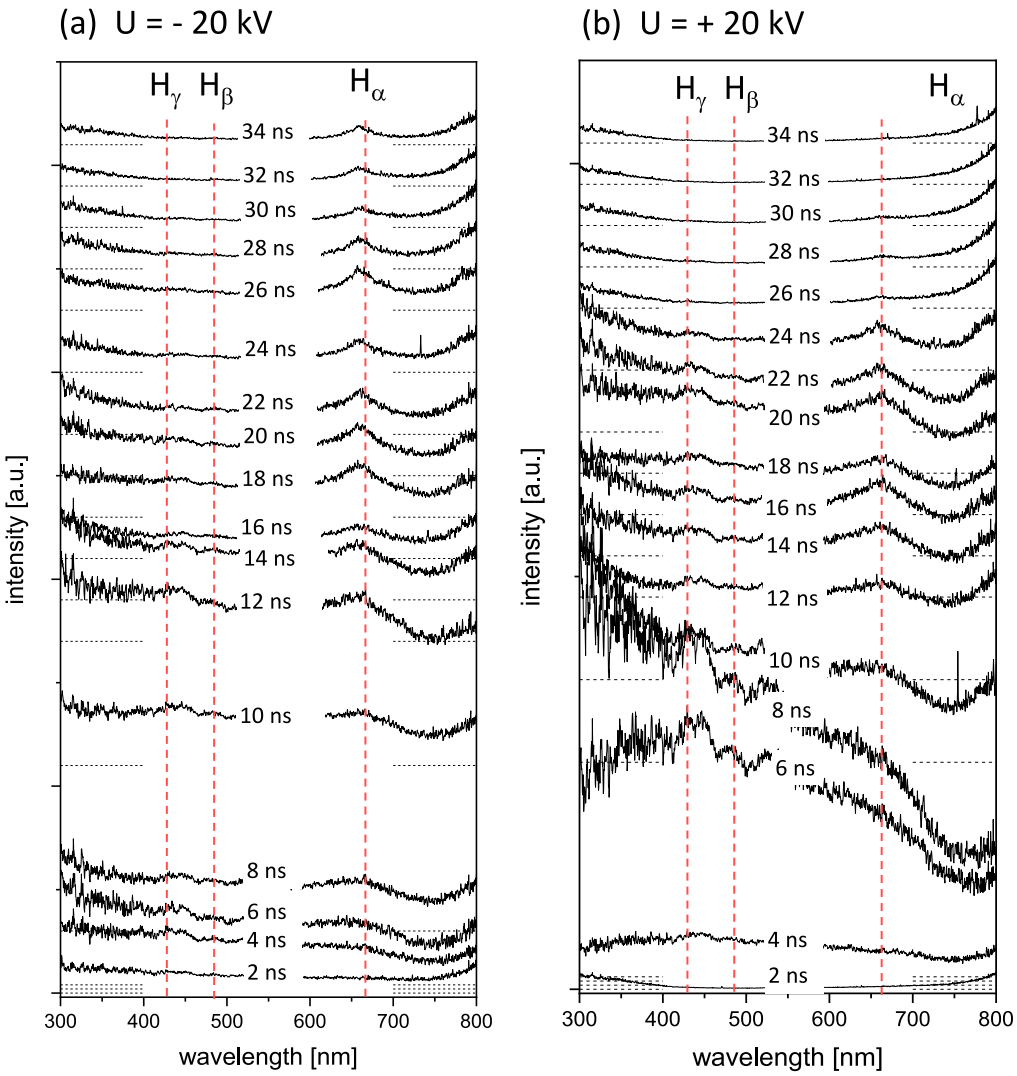

Figure 17. Temporal evolution of optical plasma emission for negative (a) and positive (b) polarity at $U = 20\,\mathrm{kV}$. The offset stacking is chosen for better visibility of the broadened emission lines H_α, H_β and H_γ (red lines).

For negative polarity, the determination of the approximate surface temperature is more difficult. The continuum radiation for the negative polarity seems to be more influenced by other processes, like e.g. hot spot radiation at the electrode in the range of smaller wavelengths or Bremsstrahlung due to the acceleration and deceleration of the electrons in connection with the ions and neutrals. As noted above, in the two-region-model a combination of hot spot radiation and black body radiation was used.

In contrast to Simek et al. [54] the combination of hot spot radiation and black body radiation fit the measured spectra in this work appropriate. This is a rough model because of the different possible continuum contributions, the large signal-to-noise ratio, especially at the short wavelengths below $< 300\,\mathrm{nm}$ and the long wavelengths

above $> 700\,\text{nm}$, respectively, as well as the rather subjective adjustment of the fitting parameters. It is assumed, that a high current on a local area at the hot W surface is forming a hot spot (violet dotted line) at $T = 20\,000\,\text{K}$, which results in the short wavelength contribution of the continuum. The continuum background (black line) results from this hot spot combined with the black body (red dotted line) contribution, which corresponds to a variable temperature (see figure 19). The approximate surface temperatures at 4 ns are $T_{20,-} = 4500\,\text{K}$ for $-20\,\text{kV}$ and $T_{16,-} = 3800\,\text{K}$ for $-16\,\text{kV}$, respectively. These temperatures at 20 kV are consistent with the observations from the SEM images in subsection 4.4.2, where clear melting traces for the negatively charged W electrode and crystallisation for the positively charged electrode are visible.

After the modelled continuum background of the radiation is subtracted from the measured data, the characteristic emission lines for H and O atoms remain (figure 31 in appendix A.3). Due to the strong line broadening, as explained in subsection 3.2.3, and the poor signal-to-noise ratio only the Balmer series with H_α, H_β and H_γ is visible in the spectra. The emission lines are modelled using a two-region model [29, 50]. This combines the emission from the two plasma regions in order to model continuum substracted data (light green). The ionisation takes place mainly in the streamer head (blue line) and the recombination in the streamer channels (orange line). The emission lines (dark green) can be fitted by adjusting the amplitude, the FWHM and the shift of the respective emission line for streamer head and channel emission, which is shown in figure 31.

The modelling of the emission lines includes self-absorption which leads to a reabsorption of the emitted photons by the surrounding hydrogen atoms along the line of sight. The model fits best for high self-absorption of the H_α line mainly in the streamer heads (ionisation region) whereas the H_β and H_γ emission can be best fit with self-absorption in the streamer channels (recombination region). By combining both region contributions, the characteristic line spectrum can be modelled for each step in time.

Figure 18 shows the number of emitted hydrogen atoms derived from the integrated line profile of H_α for 20 kV (a) and 16 kV (b) for both polarities. A strong H_α emission at the beginning of the discharge for the positive voltage pulses is prominent, while this strong light emission does not occur for negative voltage pulses. After this first high intensity, the curves for both polarities behave similarly. This evolution can be observed independently of the voltage strength, although the overall emission is significantly lower for lower voltage strengths.

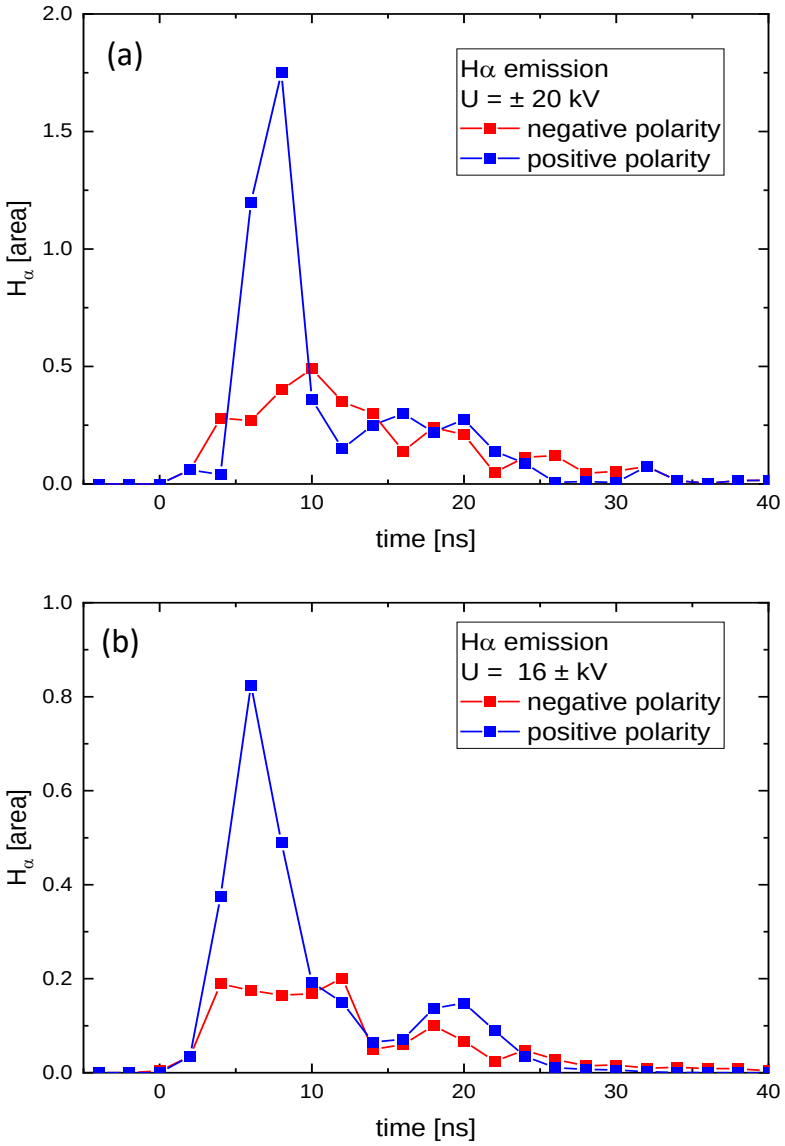

Figure 18. Development of the H_α region over time for the positive (blue) and the negative (red) pulse polarity for $U = 20\,\mathrm{kV}$ (a) and $U = 16\,\mathrm{kV}$ (b).

In the context of this work the FWHM of the H_α line Δ_{H_α} is used, to determine the resulting electron density n_e according to Kielkopf und Allard [57]:

$$\Delta_{H_\alpha}[\text{Å}] = 1.55 \cdot 10^{-11} \left(n_\mathrm{e}\left[\mathrm{cm}^{-3}\right]\right)^{0.70\pm0.03} . \tag{8}$$

This electron density evolution is shown in figure 19. It is notable that the maximum electron density for the positive polarity is higher than for the negative polarity and decreases after the intensity maximum at 4 ns for both voltage amplitudes. The electron density of the negative polarity reaches its maximum for both voltage amplitudes at 10 ns, i.e. $\Delta t = 6\,\mathrm{ns}$ later than for the positive polarity. Independent of polarity and voltage, the electron density decreases after 15 ns, which corresponds to the pulse width

and the emission intensity curve from figure 14. Furthermore, oscillations appear, which are observable in the electrode voltage pulse and in the light emission as well. Thus, the electron density, the electrical power and the brightness of the plasma seem to be coupled.

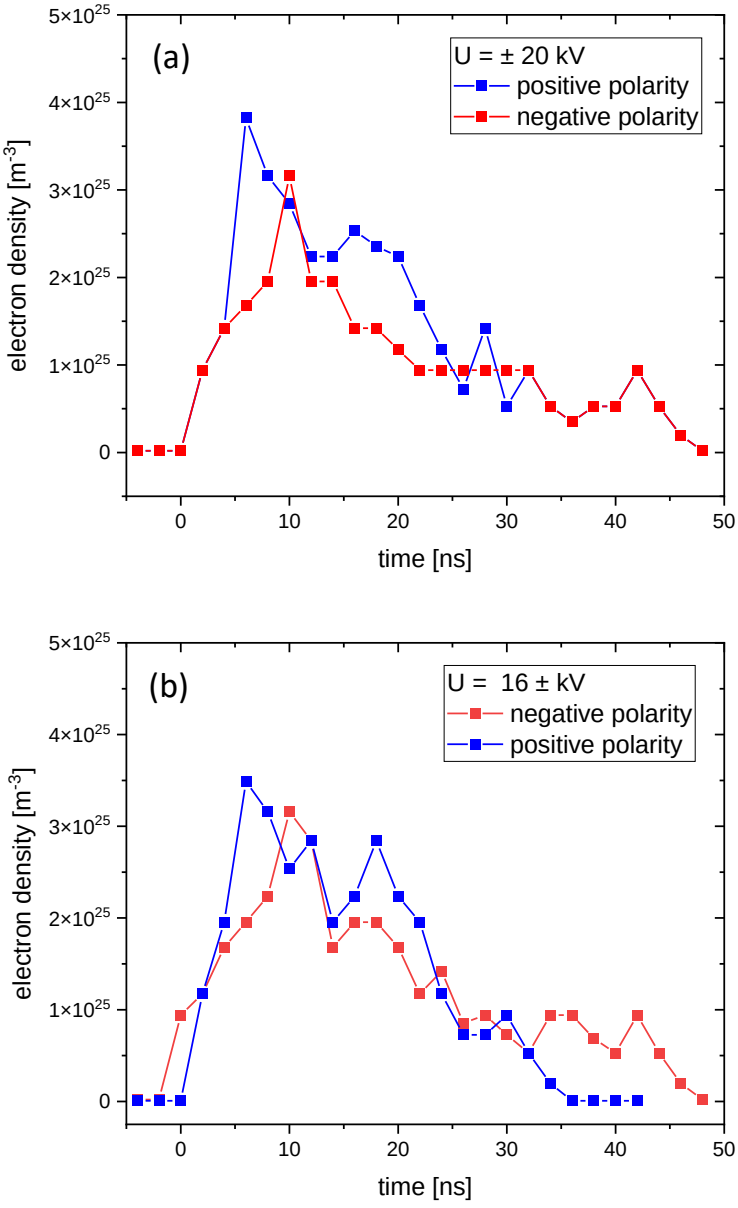

Figure 19. Electron density development over time for the positive (blue) and the negative (red) pulse polarity for $U = 20\,\mathrm{kV}$ (a) and $U = 16\,\mathrm{kV}$ (b).

All in all, the electron density seems to be independent of the voltage amplitude and develops relatively similar for positive and negative polarities except for the first maximum. This first density maximum can also be seen in the emission intensity development of the plasmas. For rising electron densities the emission intensity caused by black body radiation is higher, therefore the heating seems to be caused by the emitted electrons.

This high black body radiation is only visible for the positive pulses which could lead to the assumption, that the electrons generated by field ionisation bombarding the electrode surface are responsible for this heating. At the very beginning the positive voltage pulse causes intense light emission, while it is lower in the case of the negative polarity. Subsequently, this emitted light spectrum is again quite similar for both polarities. It can be concluded that the plasma propagation depends only minimally on the polarity of the voltage, which already excludes a discharge in a local gas bubble, because in gaseous streamer discharges, positive streamers have a much lower electron density than negative streamers [22].

However, the polarity of the voltage pulse seems to affect the ignition mechanism as can be seen in the differences in initial electron density, H_α light emission, overall light intensity and black body temperature. This difference in the initial phase of discharge for the different polarities suggests that field effects are causing the ignition. The direction of the electric field is different for the different voltage polarities. The high amount of emitted light can be explained by the occurrence of field ionisation. The ionisation of the H_2O molecules surrounding the electrode occurs quite easily, but it seems that once the plasma propagation is started, hardly any new electrons tunnel from the water molecules to the electrode. This is caused by the decrease of the electric field strength with increasing distance from the source. Due to the already ignited plasma, the distance between the not yet ionised molecules and the electrode increases and the field strength is no longer sufficient for field ionisation of water molecules during and after the falling edge of the voltage pulse. In the case of field emission the electrons can continuously escape the electrode material during the entire applied voltage pulse.

4.4 Electrode Material

In addition to the tungsten (W) electrode, platinum (Pt) and a platinum/iridium (Pt/Ir) alloy were used as electrode materials to investigate how different material properties affect plasma ignition. The alloy consists of 90 % platinum and 10 % iridium, the tungsten wire has a purity of 99.95 % and the platinum wire a purity of 99.99 %. All electrode tips were handmade from the 50 µm wire using side cutters. This can result in contamination, unevenness and cracks in the hair-width electrode tips. However, these micrometer-sized irregularities do not affect the shape, brightness or development of the plasma. For more accurate measurements, it is advisable to produce the tip in the clean room using more precise methods, such as etching, but that was not possible nor necessary within the framework of the thesis.

During the plasma discharge, the electrode erodes and for tungsten a loss rate of 1 mm/h is observed. For Pt and Pt/Ir no loss rate could be determined, due to their short lifetime for plasma initiation caused by melting of the surface [41]. A dependence of the threshold for field ionisation for different electrode materials in a water environment has been presented in [58]. If this material dependence is visible in this experiment, this would be a strong indicator that field effects generate the first electrons in the presented plasma-liquid system. While a voltage of ±20 kV is sufficient for the W wire to reliably ignite the plasma on a regular basis, ±26 kV is required for Pt/Ir and Pt, which could be caused by the different work function or the crystalline structure of the metal, especially at the surface.

For the different electrode materials the shape and the emission intensity of the plasma at negative and positive voltage polarities were observed. In addition, the transformation of the surfaces of the electrodes before and after plasma exposure was investigated.

4.4.1 Plasma Ignition

In subsection 4.1.2, the shape and the development of the plasma emission intensity over time for a W electrode was described. Now this series of measurements is repeated for Pt and Pt/Ir electrodes. The applied voltage here is ±26 kV, which is why the general brightness is higher than for the W electrode with ±20 kV. The ICCD images for Pt are shown in figure 32 and for Pt/Ir in figure 33 in appendix A.4. In these, the intensity development and streamer formation is analogous to that described for W. The local high intensity regions around the electrodes appear significantly larger and more homogeneously around the electrode, especially for Pt, but this is probably due to the higher voltage.

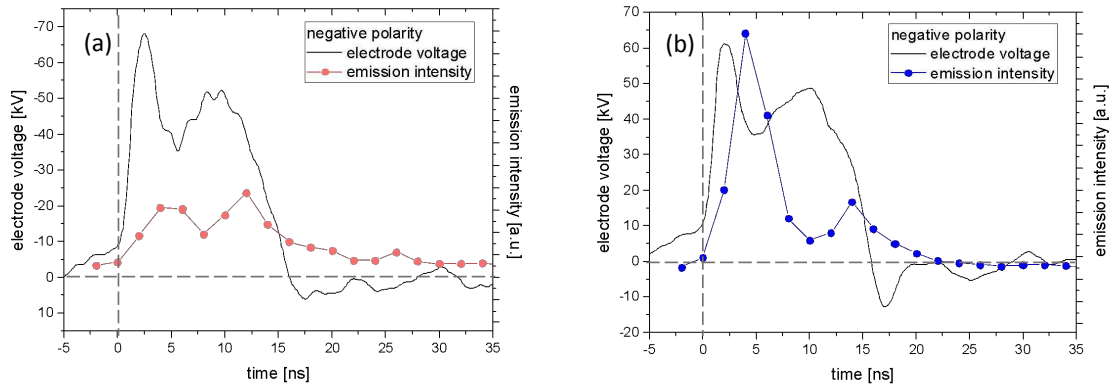

Figure 20. Integrated light intensity for the negative (a) and the positive (b) pulse polarity against time in comparison to the reconstructed voltage pulse (black) for Pt electrode and $U = 26\,\mathrm{kV}$. The dotted lines denote $t_0 = 0\,\mathrm{ns}$ and $U_0 = 0\,\mathrm{kV}$.

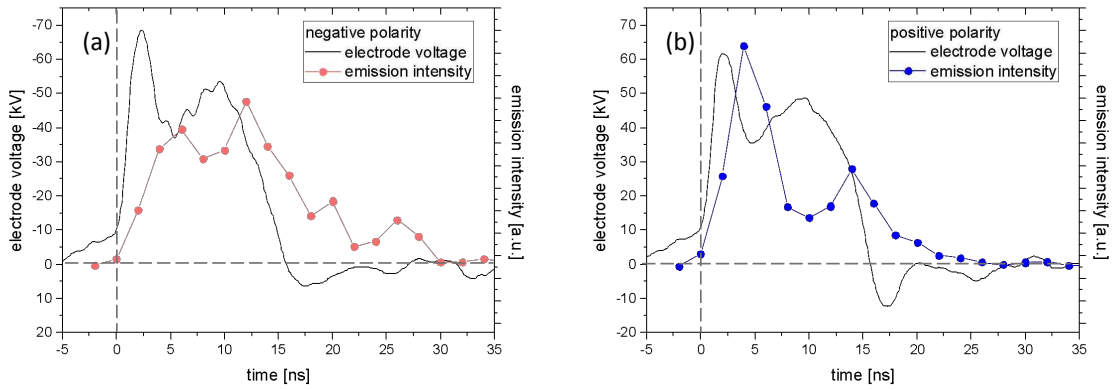

Figure 21. Integrated light intensity for the negative (a) and the positive (b) pulse polarity against time in comparison to the reconstructed voltage pulse (black) for Pt/Ir electrode and $U = 26\,\mathrm{kV}$. The dotted lines denote $t_0 = 0\,\mathrm{ns}$ and $U_0 = 0\,\mathrm{kV}$.

The emission intensity curves for Pt and Pt/Ir electrodes (see figures 20, 21) are consistent with the observations for the W electrode. For both polarities the highest intensity is reached 4 ns after ignition, while the intensity minimum takes place around 8 ns for both polarities. This is followed by another maximum in intensity until hardly any emission is observed at least for the positive polarities around 20 ns. The high overall emission intensity in figure 21 for Pt/Ir can possibly be explained by an altered metal structure due to the alloying of platinum with iridium [59]. From this comparison it can be concluded that there is no material dependence with regard to the emission intensity evolution of the discharge, but the different ignition voltage indicates possible differences caused by material structure or the work function. This is consistent with the observations that the Pt and Pt/Ir electrodes are melted by the plasma significantly faster than the W electrode [23].

4.4.2 Surface Modification

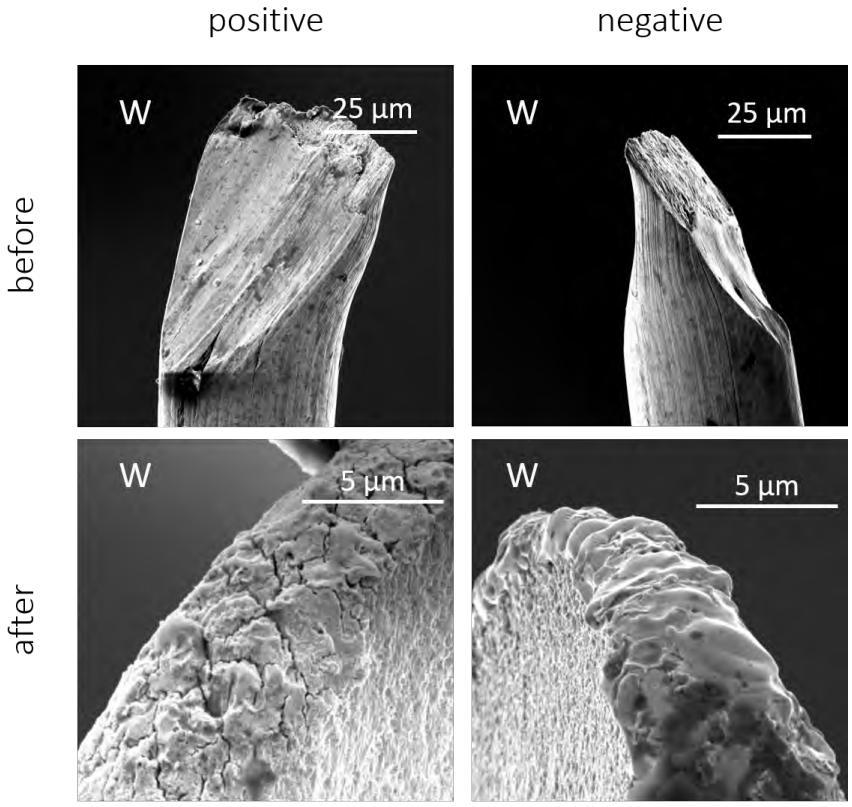

Figure 22. SEM micrographs of the W tip before (top row) and after (bottom row) plasma exposure for positive (left column) and negative (right column) pulse polarity.

If the surface of the electrodes is compared before and after plasma exposure, there are differences depending on the material, which allow conclusions to be drawn about the electrode temperature. For these measurements, six electrode tips were newly manufactured, two for each material, of which one was operated with negative polarity and one with positive polarity. Figure 22 shows the surface of the W electrode tip before (top row) and after (bottom row) plasma exposure. The positive polarity electrode (left column) was operated for 30 min with a positive voltage of +20 kV and the negative polarity electrode (right column) for 25 min with a voltage of −20 kV. The two surfaces after plasma exposure are very different from each other. The surface of the negative electrode exhibits molten and re-solidified pits, while the positive electrode shows distinct cracks instead of molten topology.

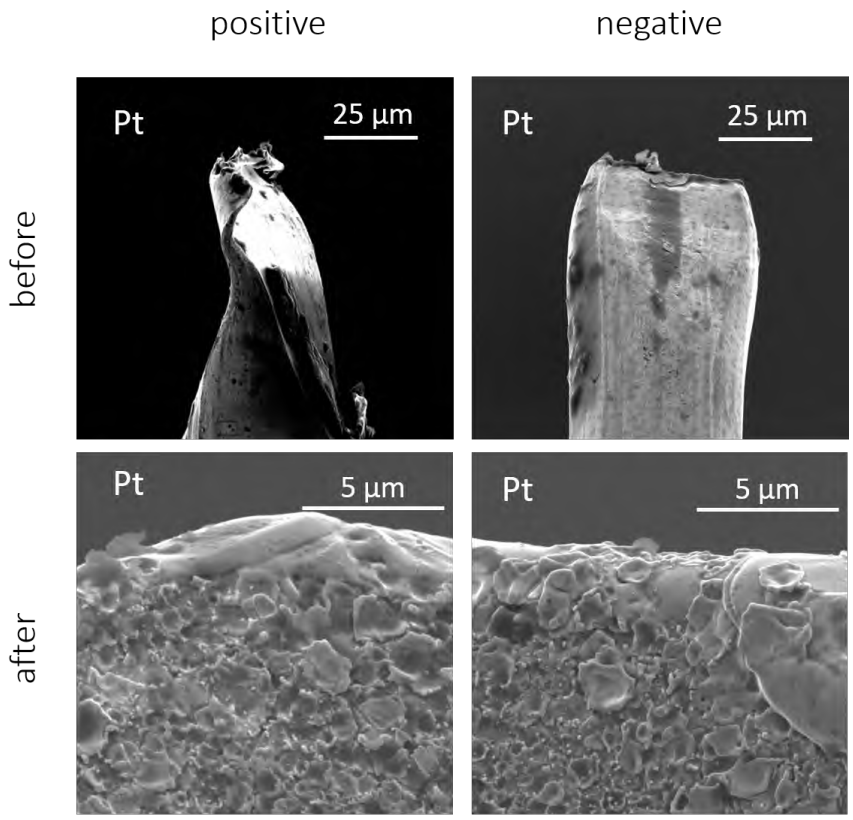

Figure 23. SEM micrographs of the Pt tip before (top row) and after (bottom row) plasma exposure for positive (left column) and negative (right column) pulse polarity.

The assumed temperature of the electrode, based on the black body radiation explained in section 4.3 fitted to the spectrum, was $T \approx 7000\,\mathrm{K}$ for $+20\,\mathrm{kV}$ and significantly lower for $-20\,\mathrm{kV}$ with approximately $T \approx 4500\,\mathrm{K}$. These temperatures are very close to the boiling and melting temperature of W, respectively, which are listed in appendix A.1 in table 1. Due to the high pressure at the beginning of ignition, the curves for boiling and melting can shift depending on the material. This effect can be described by the Clausius-Clapeyron equation, see [60]. However, the analysis of this effect exceeds the scope of this thesis. Presumably, the electrode surfaces are heated up to these phase transitions by the dissipated energy and any further energy input then causes the phase transition to occur, but does not lead to any further temperature increase.

The different surface structures fit well to the model of field effects. In case of the negative polarity, field emission causes free electrons to be emitted from the electrode into the surrounding water. This releases energy and cools the surface. Thus, only the heating of the flowing current is effective, which is sufficient to achieve the phase transition from solid to liquid. As soon as the current stops flowing, the electrode cools down and the molten topology remains visible.

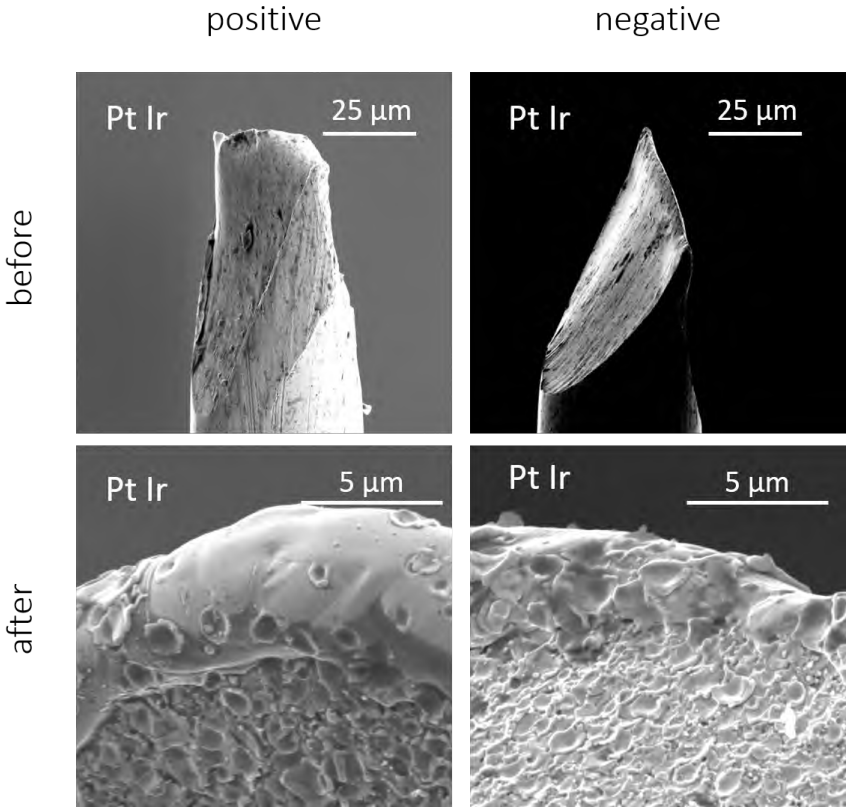

Figure 24. SEM micrographs of the Pt/Ir alloy tip before (top row) and after (bottom row) plasma exposure for positive (left column) and negative (right column) pulse polarity.

With positive polarity field ionisation occurs and the electrons tunnel from the H_2O molecules into the electrode. This can be described as a bombardment of electrons onto the surface of the electrode, which generates an enormous amount of heat. This strong heating leads the electrode to start boiling directly. The result is not a molten topology but a grainy surface with cracks. Due to the rapid heating, larger grains form and the W electrode begins to crystallise. The large inherent stress then becomes visible when the electrode cools down due to the cracking of the surface.

It is remarkable that both Pt and the Pt/Ir mixture do not show such cracks after the plasma exposure, see figures 23 and 24. Both tips were exposed for a period of 10 min and a voltage of 26 kV. This shorter period is necessary because the Pt and Pt/Ir tips are softer and melt more quickly under the influence of plasma. Instead of clear cracks, which can be seen at the surface of the W electrode, melting droplets are clearly visible on the surface of the positively charged Pt and Pt/Ir electrodes. The shape of these molten droplets is similar to the electrode surfaces exposed to negative voltage.

If the boiling and melting temperatures of Pt and the Pt/Ir mixture are compared to the temperatures of W, it is noticeable that Pt begins to melt at a temperature of $T \approx 2000\,\mathrm{K}$ and boils at $T \approx 4000\,\mathrm{K}$. Accordingly, the electrode surfaces, for both the negative and positive pulse should not exceed these temperatures. This seems unusual compared to the W electrode, to which a smaller voltage was applied. In order to draw further conclusions, it would be necessary to record the optical emission spectrum with a Pt and a Pt/Ir electrode and to model the black body radiation.

4.5 Results Compared to Ignition Models

In this section, the previous observations are collected and compared with the ignition models presented in section 2.2.

It was determined by ICCD imaging that during the plasma propagation no visible differences are observed with respect to a variation of the polarity. The visible bright areas located next to the electrode and the propagating streamers are visible for both, negative and positive polarity. Also, the variation of the electrode material has no influence on the shape of the plasma discharge.

However, for the emission intensity taken from those ICCD images a difference can be observed within the first 15 ns of plasma ignition. The plasma of the positive polarity shows a global maximum at 4 ns. The intensity then decreases to a local minimum at 8 ns and reignites more weakly at 15 ns in line with the falling edge of the voltage pulse. The emission intensity of the negative plasma pulse rises with the rising voltage edge, but does not decrease to the same amount as the positive plasma emission. The discharge reignites earlier within the voltage pulse, visible by the second maximum right before the voltage decreases at approximately 12 ns. If the position of this maximum is compared with the temporal development of the voltage pulse, a small voltage rise on the plateau of the square-wave pulse is noticeable at 12 ns, which is caused by the reflection and superposition of the pulse at the electrode tip. It is possible that this leads to the second maximum of the discharge emission.

These observations can be explained by field effects. With the negative voltage pulse, field emission would take place and electrons can tunnel out of the electrode into the water due to a deformation of the potential barrier caused by the high electric field strength. The field strength required for this depends on the electrode material. Unfortunately, there are only a few values in the literature for these thresholds under the present conditions. According to Gomer [19], a field strength of at least 0.3 - 0.6 V/Å must be reached for an emission of electrons from a W electrode with a workfunction $\Phi = 4.5$ - 5.5 eV. However, for W in H_2O was shown that a liquid environment changes the work function [58]. According to Schmidt, field ionisation of H_2O in a W electrode occurs with an applied field strength of 0.2 V/Å and a probability of 1 % to 5 %.

As long as the voltage pulse is applied to the electrode, recharging occurs and the electrons can tunnel into the liquid at any small voltage variation for negative applied voltages. Therefore, it is conceivable that the small voltage rise at 12 ns leads to electron generation from field effects, even before the voltage drops.

For the positive pulse, the second maximum seems to coincide with the falling voltage pulse and is much smaller than the first one. This can be explained, by the process of field ionisation. For positive pulse polarity, electrons from the surrounding H_2O molecules can tunnel towards the electrode. During the end of the pulse, the plasma propagated further and the next molecules that have not yet been ionised are located behind this plasma. Hence, the H_2O molecules are further away from the electrode and the electrical field strength weakens with increasing distance. Therefore, the electric field strength might not be sufficient enough to effectively trigger field ionisation.

This would also explain the behaviour after the first 15 ns of the emission intensities, where the plasma of the negative voltage pulse is clearly more susceptible to the fluctuations in the voltage pulse. This theory is supported by the analogous intensity curves at the Pt and Pt/Ir electrodes, see figures 20 and 21. Accordingly, the observation is independent of the material.

If the electron densities are now compared with the temporal development of the emission intensity, the same behaviour can be observed. The electron density is most intense for the positive voltage pulse at 4 ns, independent of the voltage amplitudes. At 15 ns, the falling edge of the voltage pulse, the electron density rises again and then falls steadily. This observation is congruent with the theory of field ionisation.

The development of the electron density for the negative polarity is also analogous to the emission intensity. The observed maxima occur at the same points in time (4 ns and 12 ns) and in the time frame of 15 - 35 ns the intensity fluctuations match the voltage fluctuations. This observation corresponds to the previously described emission intensity and can be explained by field effects.

The determined black body temperature also supports the ignition via field effects. Here, higher electrode temperatures up to $T = 7000\,\mathrm{K}$ are determined for the positive W electrode. In the case of the negative voltage, the continuum radiation cannot be fitted as clearly as the positive pulse spectra. The black body radiation can only be fitted for lower temperatures $T < 4500\,\mathrm{K}$. These results are also consistent with the SEM imaging of the W electrode before and after plasma treatment. After the exposure to a negative voltage pulse, clear molten structures are visible on the surface, but after the exposure to a positive voltage pulse, clear cracks are shown, which presumably originate from a previous crystallisation. Regarding the Clausius-Clapeyron equation, which describes the shifted phase transitions of a material due to high pressure [60], it is possible that, the phase transition from solid to liquid is reached for the negative voltage and the transition from liquid to gas for the positive voltage pulse. This could also explain the visible different surface structures, see figure 22. For Pt and Pt/Ir, these different surface structures are not apparent, only molten droplets are visible at the surfaces after the plasma exposure for both polarities. Figures 23 and 24 show both molten electrode surfaces which indicates that only the phase transition from solid to liquid is reached, but not the boiling temperature, independent of the pulse polarity. This could be explained by the different material structure or by the shift of the melting point at high pressures in the range of GPa [60] which are determined for these nanosecond plasmas in liquids. Another possible explanation is, that the different work functions and Fermi-levels of the materials influence the different field effects. Different thresholds for field ionisation have been published for W/H_2O (20 MV/cm), Ir/H_2O (51 MV/cm) and Pt/H_2O (61 MV/cm) systems. It is reported, that for the same ion currents, the field strength of Pt/H_2O systems needs to be approximately three times higher than for W/H_2O [58]. Therefore, more energy is needed for field ionisation of the Pt/H_2O and less energy can be deposited in heating the electrode.

The decay of the spectrum after the HV pulse is almost identical for both polarities. This also applies accordingly to the electron density. The almost identical decay rate could correspond to the loss of electrons due to recombination of electrons with ions, which indicates that the densities are similar for both polarities, as can be seen in figure 19. It can be concluded from the temporal evolution of the electron densities that the ignition mechanisms are polarity-dependent, but the plasma propagation is

independent of the voltage pulse polarity. In addition to the electron densities for different voltages, this independence of polarity is also visible in the emission intensities (figures 14, 20, 21) and in the ICCD images (figures 13, 32, 33). This conclusion is also supported by the cavitation bubble shadowgraphs, shown in appendix A.2, where no difference in bubble shape or in the bubble radius development can be found for the different polarities (compare figure 15). This leads to the assumption that the same energy is dissipated into the discharge. The cavitation bubble and the gas channels remaining from the discharges should therefore be directly correlated to the dissipated energy. This can be supported by the BCS measurements used for energy determination showing very similar energies of 12 mJ and 18 mJ for W at both polarities.

The observation that ignition induces a polarity dependence, but propagation is independent of the electric field direction, is in contradiction to the observations of Seepersad et al. [33], who found very different emission patterns for the emission of a positive and negative pulsed discharge in distilled water. According to Seepersad et al. the negative pulsed discharge resulted in a weakly glowing structure at the electrode, whereas a positive pulse resulted in a filamentary discharge structure. This was explained by a gas-like characteristic. Although the experimental setups are comparable, the observations differ significantly, which cannot simply be explained by the longer rise times with 4 ns and the used pin-to-plate electrode setup.

The observation that the ignition is polarity-dependent and the propagation is polarity-independent can be explained by a possible combination of field effects with a low density region, such as nanovoids or a supercritical fluid. Such a combination was also supposed by T. Lewis, who was the first to postulate the creation of nanovoids in those liquid discharge systems [37]. Different voltages would influence the formation of nanovoids, weaker electric fields cause less electrostriction. Different polarities would reverse the direction in which the electrons are accelerated, which could possibly be seen in the form of plasma propagation. Whereas, different electrode materials should not have an effect on the formation of the nanovoids, as their formation is independent of the work function and Fermi level of the electrode material.

The formation of an SCF at the beginning of the ignition is a possible model to explain the discharge in nanosecond pulsed plasmas. A SCF is created in an environment of high pressure and temperature which can both occur for these plasmas [23, 29, 49]. A change in voltage amplitude of a few kV would not change these values to such an extent that temperature or pressure would fall below the super critical state in the phase

diagram of water. Different materials of the electrode would not suggest differences in propagation, except for differences in ignition due to field effects. A different polarity of the voltage may results in a direct difference in the propagation of the plasma, as the electrons would be accelerated either towards or away from the electrode.

The observed lower emission intensity for the ±16 kV compared to the ±20 kV can be explained for both theories equally by the higher temperature of the electrode and the associated smaller continuum radiation. There are no observed differences in the ICCD images of the plasma propagation for the different polarities, therefore it is possible that the plasma streamers occur independently of the direction in which the electrons are accelerated. The fact that no differences in plasma propagation are observed for different materials speaks for both the supercritical fluid and the nanovoids. The differences in the change of the electrode surface after discharge ignition can be explained by the field effects. The only observation that favours an SCF over nanovoids is the high electron density directly at the rising edge of the voltage pulse for the positive voltage polarity. For ignitions within gas(-like) environments, the electron density for negative pulses is usually higher than for positive [22].

5 Conclusion and Outlook

The discharge of nanosecond pulsed high voltage plasmas in liquids was considered for different polarities. Special attention was paid to the ignition mechanism and plasma propagation. Due to very short voltage rise times of 2-3 ns the inertia of the liquid is too high to react to the pressure gradient induced by the applied electric field. No gas environment can be created in which the plasma ignites, as it would occur for voltage pulses with longer rise times. Within the framework of this work, current theoretical models were experimentally studied with respect to ignition behaviour, streamer evolution, bubble formation and electrical characteristics. Different voltage polarities and amplitudes from 16 - 26 kV and different electrode materials (W, Pt, Ir) were used.

Using BCS measurements, the shape of the voltage pulse at the electrode tip was determined by superposing the initial voltage pulse with the reflected pulse. The energy dissipating in the plasma was calculated to 12 mJ for the positive pulse and 18 mJ for the negative pulse. For a more accurate determination of the pulse shape and the dissipated energy, a model of the pulse would be needed, taking into account all mismatched impedances at which a reflection of the voltage pulse appears.

Optical diagnostics such as ICCD imaging and optical emission spectroscopy were used to observe the temporal development of the emission intensity during the discharge. A correlation between the voltage pulse and the emission intensity was found. With rising and falling edges, the plasma ignites presumably due to the onset of field effects. With positive polarity, this first maximum is clearly more intense than for ignition with negative polarity. The black body radiation (corresponding to $T = 7000\,\mathrm{K}$), H_α region and electron densities ($n_e = 4 \times 10^{25}/\mathrm{m}^3$) are more intense for ignition with positive polarity as well. For negative polarity, black body radiation for a lower temperature around 4500 K is emitted, while more other radiation sources contribute to the continuum spectra. The overall emission intensity has two approximately equal maxima at the beginning and towards the end of the voltage pulse. These are significantly weaker in intensity than the maxima at the positive polarity. This is the same for all observed materials.

The recorded ICCD photographs show the same formation of streamer branches and particularly bright regions directly at the plasma electrode, which are presumably caused by black body radiation. After ignition, the electron densities also show the same decay behaviour, which indicates a polarity-independent propagation of the plasma. The behaviour of the decreasing electron densities and the H_α regions has been observed for $\pm 20\,\mathrm{kV}$ and $\pm 16\,\mathrm{kV}$.

From the SEM images before and after plasma exposure, different surface modifications for different materials can be observed. While the tungsten electrode ignites regularly from 20 kV, a voltage of 26 kV is required for Pt and Pt/Ir, caused by different field effect thresholds and surface structures of the metals. There are clear signs of melting on the surface of all electrodes, except for the positive tungsten electrode, where boiling structures are visible. This can be explained by different surface temperatures, different material structures and thresholds. In view of this observation, an analysis of the emission spectrum for Pt and Pt/Ir would be useful to further investigate the relationship between black body temperature, electron density and material threshold.

After the discharge, a cavitation bubble is formed, which was monitored using shadowgraphy. The evolution of the bubble radii was modelled according to the simplified Rayleight-Plesset equation and resulted in almost identical initial pressures inside the cavitation bubble for both polarities. This is congruent with the same dissipated energy and the similar streamers evolution for both polarities, since the cavitation bubble occurs by contracting gas channels at the previous regions of streamer branches.

Summarising all observations support a combined mechanism in which field effects are responsible for plasma ignition and following propagation inside low density regions, either SCFs or nanovoid regions. Due to the complex physics on short time and small spatial scales, the two theoretical models cannot be substantiated with experimental data. However, in all measurements taken, evidence for ignition by field effects is observable.

To draw further conclusions simulations of the solid body properties in combination with the prevailing pressures and temperatures are required. Another step would be an investigation of optical emission spectra for different metal electrodes or alloys and dopants.

Investigating acoustic waves or shock fronts occurring at the tip of the electrode could help drawing further conclusions about the pressure during ignition and thus differentiate between SCF and nanovoids. Modelling the exact voltage pulse shape can help to determine the correlation of emission and voltage changes. This model could also give more accurate values for the dissipated energies.

To evolve the most effective setup for possible industrial applications is a future goal for plasma in liquids. So far, only tungsten is suitable for a longer and possibly large-scale application. Even after longer treatment, tungsten ignites more reliable and does not melt as quickly as platinum or platinum iridium. Tungsten can also be operated at a lower voltage and therefore probably consumes less power. Which polarity is better suited for industrial applications can be determined by further and more precise observations in the future.

Bibliography

[1] S. Whitehead and E. B. Wedmore. *Dielectric phenomena : electrical discharges in liquids*. London: Ernest Benn Ltd., 1928. 137 pp.

[2] P. B. et al. 'Plasma-liquid interactions: A review and roadmap'. English. In: *Plasma Sources Science and Technology* **25**.5 (2016). ISSN: 0963-0252.

[3] D. Mariotti et al. 'Plasma–Liquid Interactions at Atmospheric Pressure for Nanomaterials Synthesis and Surface Engineering'. In: *Plasma Processes and Polymers* **9**.11-12 (2012), pp. 1074–1085.

[4] T. Kaneko et al. 'Novel Gas-Liquid Interfacial Plasmas for Synthesis of Metal Nanoparticles'. In: *Plasma Processes and Polymers* **6**.11 (2009), pp. 713–718.

[5] J. Foster et al. 'Perspectives on the Interaction of Plasmas With Liquid Water for Water Purification'. In: *IEEE Transactions on Plasma Science* **40**.5 (2012), pp. 1311–1323.

[6] S. Horikoshi and N. Serpone. 'In-liquid plasma: a novel tool in the fabrication of nanomaterials and in the treatment of wastewaters'. In: *RSC Adv.* **7** (75 2017), pp. 47196–47218.

[7] G. R. Stratton et al. 'Plasma-based water treatment: Conception and application of a new general principle for reactor design'. In: *Chemical Engineering Journal* **273** (2015), pp. 543–550. ISSN: 1385-8947.

[8] H. Krause et al. 'Degradation of persistent pharmaceuticals in aqueous solutions by a positive dielectric barrier discharge treatment'. In: *Journal of Electrostatics* **69**.4 (2011), pp. 333–338. ISSN: 0304-3886.

[9] H. Jablonowski and T. von Woedtke. 'Research on plasma medicine-relevant plasma–liquid interaction: What happened in the past five years?' In: *Clinical Plasma Medicine* **3**.2 (2015). Plasma-Liquid Interactions, pp. 42–52. ISSN: 2212-8166.

[10] K.-D. Weltmann and T. von Woedtke. 'Plasma medicine—current state of research and medical application'. In: *Plasma Physics and Controlled Fusion* **59**.1 (2016), p. 014031.

[11] N. Kumar et al. 'The action of microsecond-pulsed plasma-activated media on the inactivation of human lung cancer cells'. In: *Journal of Physics D: Applied Physics* **49**.11 (2016), p. 115401.

[12] W. Graham and K. Stalder. 'Plasmas in liquids and some of their applications in nanoscience'. In: *Journal of Physics D: Applied Physics* **44**.17 (May 2011), p. 174037.

[13] F. Seferoglu. 'Surface Modification of a Copper Substrate through the Reaction Chemistry Generated by Pulsed Plasmas in Water'. In: *Bachelor Thesis at Ruhr-Universität Bochum* (2019).

[14] P. Šunka. 'Pulse electrical discharges in water and their applications'. In: *Physics of Plasmas* **8**.5 (2001), pp. 2587–2594.

[15] H. M. Jones and E. E. Kunhardt. 'Development of pulsed dielectric breakdown in liquids'. In: *Journal of Physics D: Applied Physics* **28**.1 (1995), pp. 178–188.

[16] Y. Seepersad, A. Fridman and D. Dobrynin. 'Anode initiated impulse breakdown in water: the dependence on pulse rise time for nanosecond and sub-nanosecond pulses and initiation mechanism based on electrostriction'. In: *Journal of Physics D: Applied Physics* **48**.42 (2015), p. 424012.

[17] M. N. Shneider and M. Pekker. 'Pre-breakdown processes in a dielectric fluid in inhomogeneous pulsed electric fields'. In: *Journal of Applied Physics* **117**.22 (2015), p. 224902.

[18] P. Bruggeman and C. Leys. 'Non-thermal plasmas in and in contact with liquids'. In: *Journal of Physics D: Applied Physics* **42**.5 (2009), p. 053001.

[19] R. Gomer. 'Field emission and field ionization in condensed phases'. In: *Accounts of Chemical Research* **5**.2 (1972), pp. 41–48.

[20] X. Lu et al. 'Spark model of pulsed discharge in water'. In: *Journal of Applied Physics* **91** (2002), pp. 24–31.

[21] A. Yamatake et al. 'Characteristics of Pulsed Arc Electrohydraulic Discharge for Eccentric Electrode Cylindrical Reactor using Phosphate-Buffered Saline Water'. In: *Japanese Journal of Applied Physics* **45**.10B (2006), pp. 8298–8301.

[22] S. Nijdam, J. Teunissen and U. Ebert. 'The physics of streamer discharge phenomena'. English. In: *Plasma Sources Science and Technology* **29**.10 (2020). ISSN: 0963-0252.

[23] K. Grosse, V. S.-v. der Gathen and A. von Keudell. 'Nanosecond pulsed discharges in distilled water: I. Continuum radiation and plasma ignition'. In: *Plasma Sources Science and Technology* **29**.9 (2020), p. 095008.

[24] A. Starikovskiy et al. 'Non-equilibrium plasma in liquid water: dynamics of generation and quenching'. In: *Plasma Sources Science and Technology* **20**.2 (2011), p. 024003.

[25] W. An, K. Baumung and H. Bluhm. 'Underwater streamer propagation analyzed from detailed measurements of pressure release'. In: *Journal of Applied Physics* **101**.5 (2007), p. 053302.

[26] A. Sharma et al. 'A Preliminary Study of Pulsed Streamer Corona Discharge for the Degradation of Phenol in Aqueous Solutions'. In: *Hazardous Waste and Hazardous Materials* **10**.2 (1993), pp. 209–219.

[27] D. Dobrynin et al. 'Non-equilibrium nanosecond-pulsed plasma generation in the liquid phase (water, PDMS) without bubbles: fast imaging, spectroscopy and leader-type model'. In: *Journal of Physics D: Applied Physics* **46**.10 (2013), p. 105201.

[28] Y. Seepersad et al. 'On the electrostrictive mechanism of nanosecond-pulsed breakdown in liquid phase'. In: *Journal of Physics D: Applied Physics* **46**.16 (2013), p. 162001.

[29] K. Grosse et al. 'Nanosecond plasmas in water: ignition, cavitation and plasma parameters'. In: *Plasma Sources Science and Technology* **28**.8 (2019), p. 085003.

[30] A. Vogel, S. Busch and U. Parlitz. 'Shock wave emission and cavitation bubble generation by picosecond and nanosecond optical breakdown in water'. In: *The Journal of the Acoustical Society of America* **100**.1 (1996), pp. 148–165.

[31] D. V. Tereshonok et al. 'Pre-breakdown phenomena and discharges in a gas-liquid system'. In: *Plasma Sources Science and Technology* **27**.4 (2018), p. 045005.

[32] A. H. Sharbaugh, J. C. Devins and S. J. Rzad. 'Progress in the Field of Electric Breakdown in Dielectric Liquids'. In: *IEEE Transactions on Electrical Insulation* **EI-13**.4 (1978), pp. 249–276.

[33] Y. Seepersad et al. 'Investigation of positive and negative modes of nanosecond pulsed discharge in water and electrostriction model of initiation'. In: *Journal of Physics D: Applied Physics* **46**.35 (2013), p. 355201.

[34] Y. Li et al. 'Towards an improved understanding of nanosecond-pulse discharge initiation in water: from cavitation to electron multiplication'. In: *Plasma Sources Science and Technology* **29**.7 (2020), p. 075005.

[35] M. N. Shneider and M. Pekker. 'Dielectric fluid in inhomogeneous pulsed electric field'. In: *Phys. Rev. E* **87** (4 2013), p. 043004.

[36] A. C. Aghdam and T. Farouk. 'Multiphysics simulation of the initial stage of plasma discharge formation in liquids'. In: *Plasma Sources Science and Technology* **29**.2 (2020), p. 025011.

[37] T. J. Lewis. 'Breakdown initiating mechanisms at electrode interfaces in liquids'. In: *IEEE Transactions on Dielectrics and Electrical Insulation* **10**.6 (2003), pp. 948–955.

[38] R. H. Fowler and L. Nordheim. 'Electron Emission in Intense Electric Fields'. In: *Proceedings of the Royal Society of London. Series A, Containing Papers of a Mathematical and Physical Character* **119**.781 (1928), pp. 173–181. ISSN: 09501207.

[39] J. F. Kolb et al. 'Streamers in water and other dielectric liquids'. In: *Journal of Physics D: Applied Physics* **41**.23 (2008), p. 234007.

[40] W. Franz. 'Zener-Effekt und Stoßionisation'. In: *Semiconductors and Phosphors /Proceedings of the International Colloquium 1956„Semiconductors and Phosphors" at Garmisch-Partenkirchen*. Ed. by M. Schön and H. Welker. Wiesbaden: Vieweg+Teubner Verlag, 1958, pp. 317–328. ISBN: 978-3-663-02557-3.

[41] K. Grosse. 'Discharge ignition, dynamics and chemistry of nanosecond pulsed plasmas in water'. In: *Dissertation at Ruhr-Universität Bochum* (2020).

[42] S. Stauss, H. Muneoka and K. Terashima. 'Review on plasmas in extraordinary media: Plasmas in cryogenic conditions and plasmas in supercritical fluids'. English. In: *Plasma Sources Science and Technology* **27**.2 (2018). ISSN: 0963-0252.

[43] G. Simeoni, T. Bryk and F. e. a. Gorelli. 'The Widom line as the crossover between liquid-like and gas-like behaviour in supercritical fluids'. In: *Nature Physics* **6** (2010). ISSN: 1745-2481.

[44] H. Muneoka et al. 'Micrometer-scale electrical breakdown in high-density fluids with large density fluctuations: Numerical model and experimental assessment'. In: *Phys. Rev. E* **91** (4 2015), p. 042316.

[45] K. Nishikawa and T. Morita. 'Fluid behavior at supercritical states studied by small-angle X-ray scattering'. In: *The Journal of Supercritical Fluids* **13**.1 (1998), pp. 143–148. ISSN: 0896-8446.

[46] K. Nishikawa et al. 'Density fluctuation of a van der Waals fluid in supercritical state'. In: *The Journal of Chemical Physics* **118**.3 (2003), pp. 1341–1346.

[47] A. Kalinichev and S. Churakov. 'Size and topology of molecular clusters in supercritical water: a molecular dynamics simulation'. In: *Chemical Physics Letters* **302**.5 (1999), pp. 411–417. ISSN: 0009-2614.

[48] M.Kai. 'Optical Analysis of a Nanosecond Plasma Inside Liquids'. In: *Bachelor Thesis at Ruhr-Universität Bochum* (2018).

[49] L. Chauvet et al. 'Chemistry in nanosecond plasmas in water'. In: *Plasma Processes and Polymers* **17**.6 (2020), p. 1900192.

[50] A. von Keudell, K. Grosse and V. S.-v. der Gathen. 'Nanosecond pulsed discharges in distilled water-Part II: line emission and plasma propagation'. In: *Plasma Sources Science and Technology* **29**.8 (2020), p. 085021.

[51] P. Bruggeman et al. 'Characterization of a direct dc-excited discharge in water by optical emission spectroscopy'. In: *Plasma Sources Science and Technology* **18**.2 (2009), p. 025017.

[52] D. Staack et al. 'Nanoscale Corona Discharge in Liquids, Enabling Nanosecond Optical Emission Spectroscopy'. In: *Angewandte Chemie International Edition* **47**.42 (2008), pp. 8020–8024.

[53] P. Bílek et al. 'Electron-neutral bremsstrahlung radiation fingerprints the initial stage of nanoseconddischarge in liquid water'. In: *Plasma Sources Science and Technology* (2021).

[54] M. Šimek et al. 'Luminous phase of nanosecond discharge in deionized water: morphology, propagation velocity and optical emission'. In: *Plasma Sources Science and Technology* **26**.7 (2017), 07LT01.

[55] H. R. Griem. 'Principles of Plasma Spectroscopy'. In: *Cambridge Monographs on Plasma Physics* (1997).

[56] G. D. Danilatos. 'Introduction to the ESEM instrument'. In: *Microscopy Research and Technique* **25**.5-6 (1993), pp. 354–361.

[57] J. F. Kielkopf and N. F. Allard. 'Shift and width of the Balmer series H alpha line at high electron density in a laser-produced plasma'. In: *Journal of Physics B: Atomic, Molecular and Optical Physics* **47**.15 (2014), p. 155701.

[58] W. A. Schmidt. 'Massenspektrometrische Untersuchung der Feldionisation von Wasserdampf an Spitzen aus Wolfram, Platin und Iridium'. In: *Zeitschrift für Naturforschung A* **19**.3 (01 Mar. 1964), pp. 318–327.

[59] H. Baker. 'ASM Handbook, Volume 3: Alloy Phase Diagrams'. In: (1992).

[60] R. Clausius. 'Ueber die bewegende Kraft der Wärme und die Gesetze, welche sich daraus für die Wärmelehre selbst ableiten lassen'. In: *Annalen der Physik* **155**.3 (1850), pp. 368–397.

[61] M. Winter. 'WebElements: The periodic table'. In: *The University of Sheffield and WebElements Ltd, UK* ().

A Appendix

A.1 Material Properties

Table 1. Material properties of the metals used as electrode material, taken from [61]

Property [unit]	Tungsten	Platin	Iridium
Melting point [K]	3695	2041,4	2739
Boiling point [K]	6203	4100	4403
Enthalpy of fusion $[\frac{\mathrm{kJ}}{\mathrm{mol}}]$	35,2	19,6	26
Specific heat capacity $[\frac{\mathrm{J}}{\mathrm{kg\,K}}]$	138	130	130
Work function [eV]	4,55	5,65	5,67
Electrical conductivity $[\frac{\mathrm{A}}{\mathrm{V\,m}}]$	$1,85 \times 10^7$	$9,48 \times 10^6$	$1,97 \times 10^7$
Thermal conductivity $[\frac{\mathrm{W}}{\mathrm{mK}}]$	170	72	150
First ionisation energy [eV]	7,86	8,95	8,96

A.2 Bubble Evolution

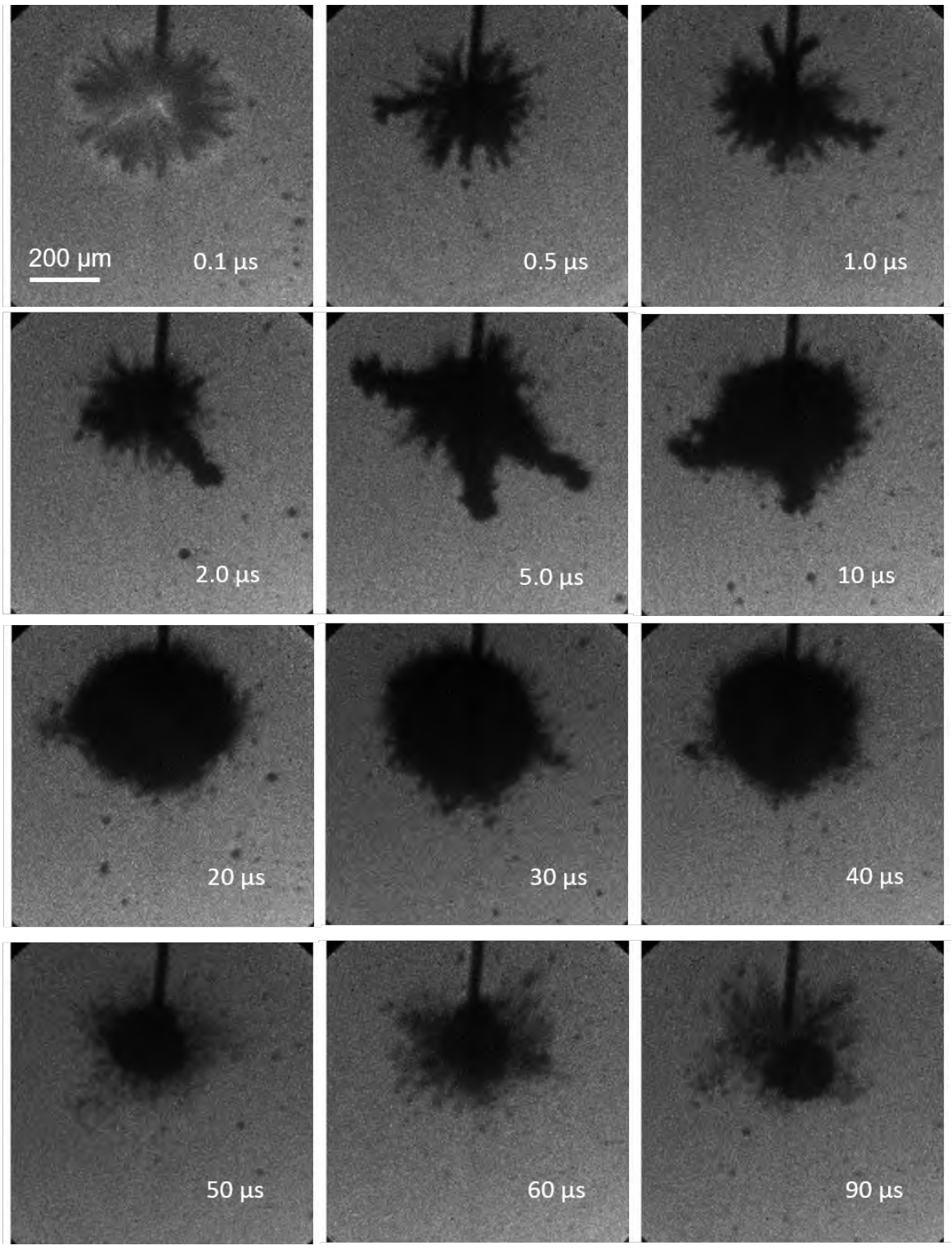

Figure 25. Time resolved shadowgraphy images of the bubble evolution for a tungsten electrode with $U = +20\,\mathrm{kV}$ and a gate time width of $t_{\mathrm{gate}} = 50\,\mathrm{ns}$.

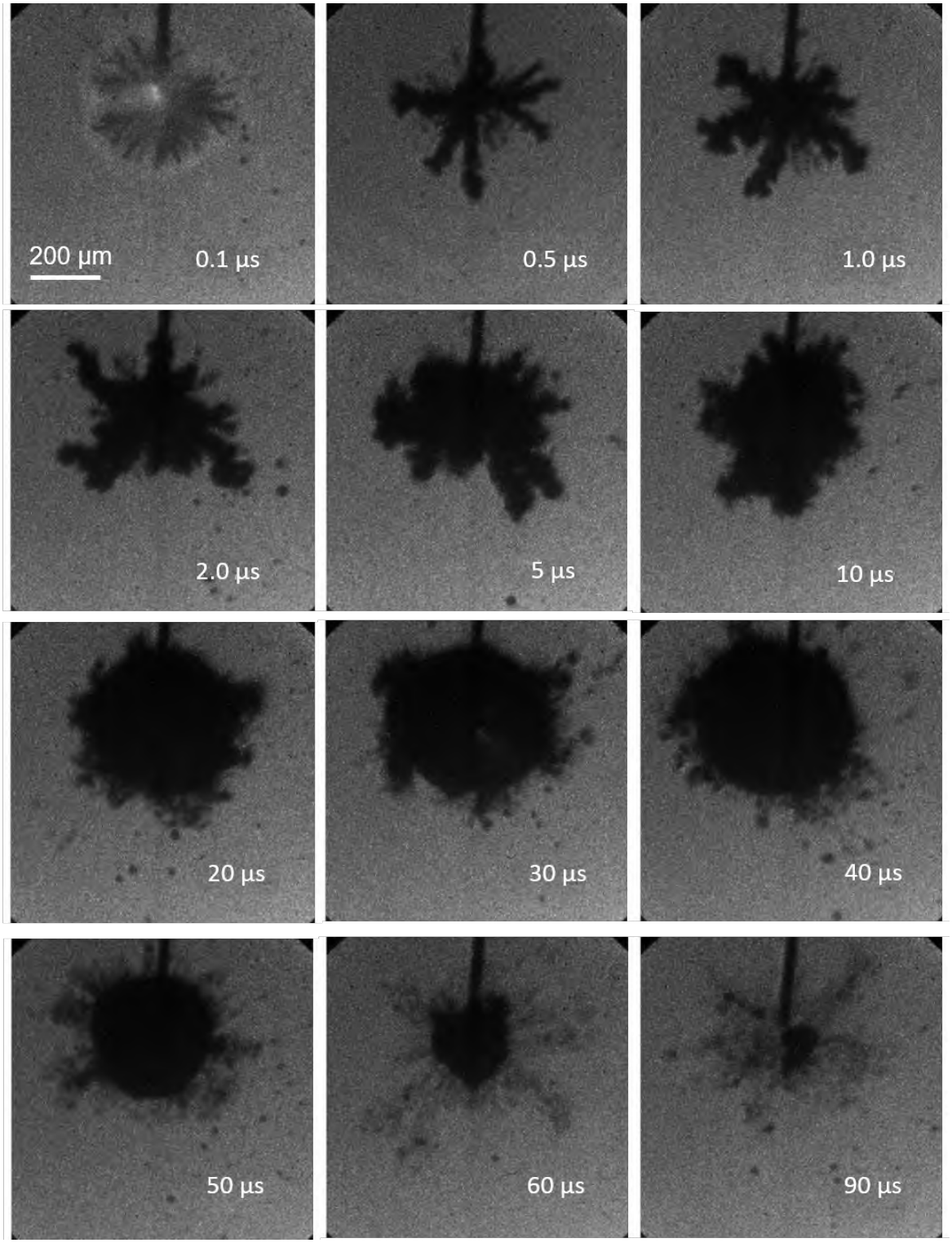

Figure 26. Time resolved evolution of the bubble shadowgraphy for a tungsten electrode with U = -20 kV and a gate time width of $t_{\mathrm{gate}} = 50$ ns.

A.3 Time-Resolved Emission Spectra

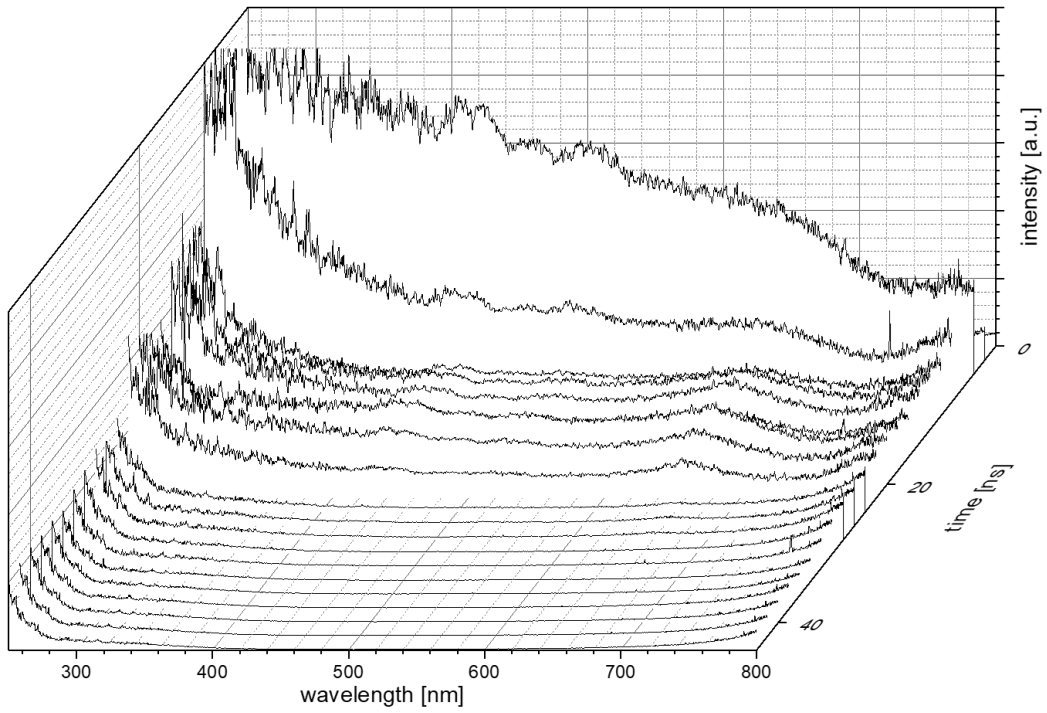

Figure 27. Temporal evolution of optical emission spectra of the tungsten electrode for $U = +20\,\mathrm{kV}$, a gate time width of $t_{\mathrm{gate}} = 2\,\mathrm{ns}$ and 2000x accumulations.

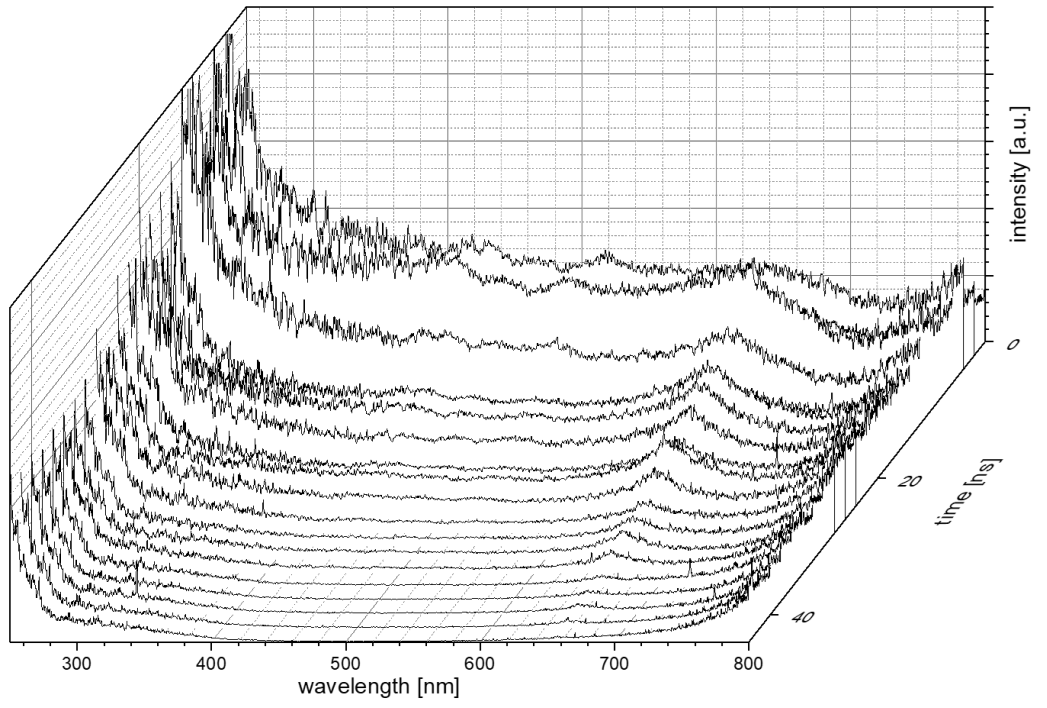

Figure 28. Temporal evolution of optical emission spectra of the tungsten electrode for $U = $ -20 kV, a gate time width of $t_{\mathrm{gate}} = 2\,\mathrm{ns}$ and 2000x accumulations.

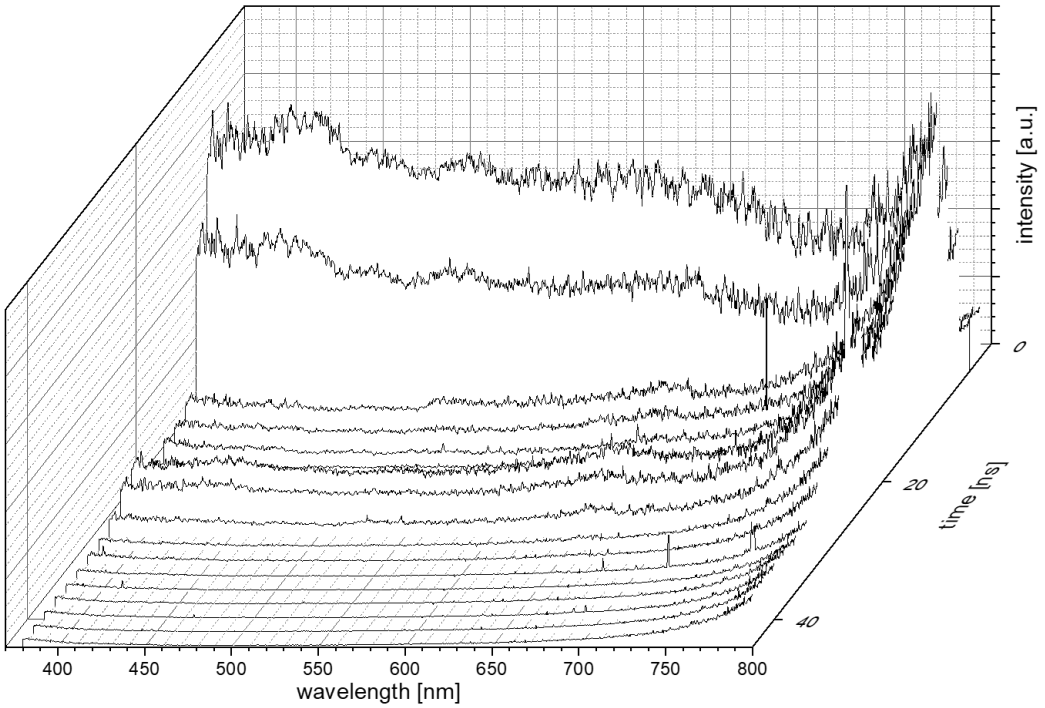

Figure 29. Temporal evolution of optical emission spectra of the tungsten electrode for $U = +16\,\mathrm{kV}$, a gate time width of $t_{\mathrm{gate}} = 2\,\mathrm{ns}$ and 2000x accumulations.

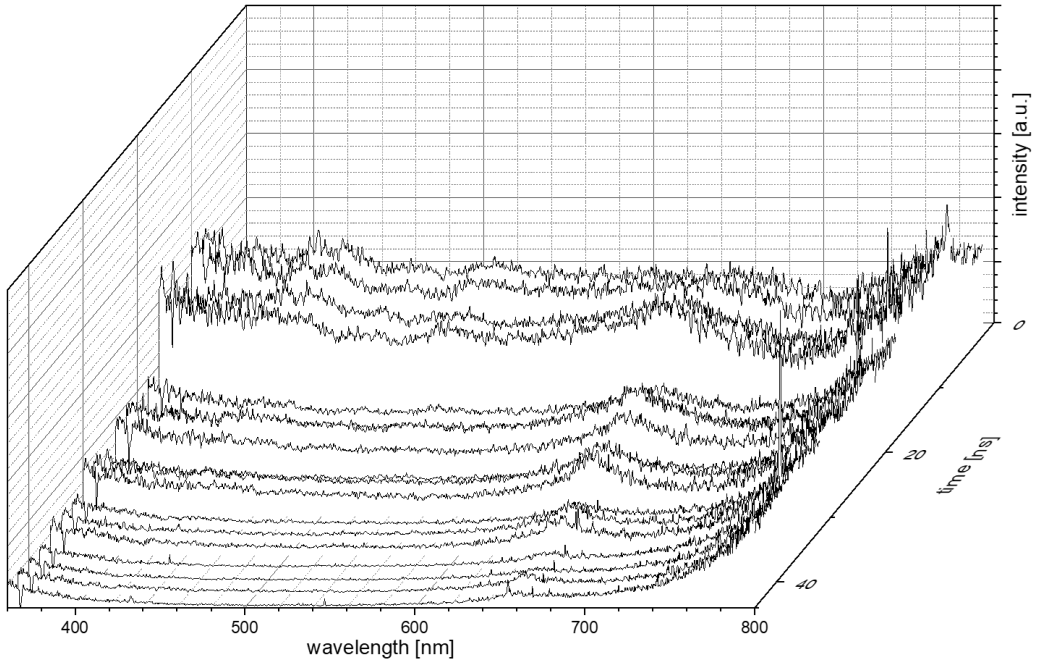

Figure 30. Temporal evolution of optical emission spectra of the tungsten electrode for $U = \text{-}16\,\mathrm{kV}$, a gate time width of $t_{\mathrm{gate}} = 2\,\mathrm{ns}$ and 2000x accumulations.

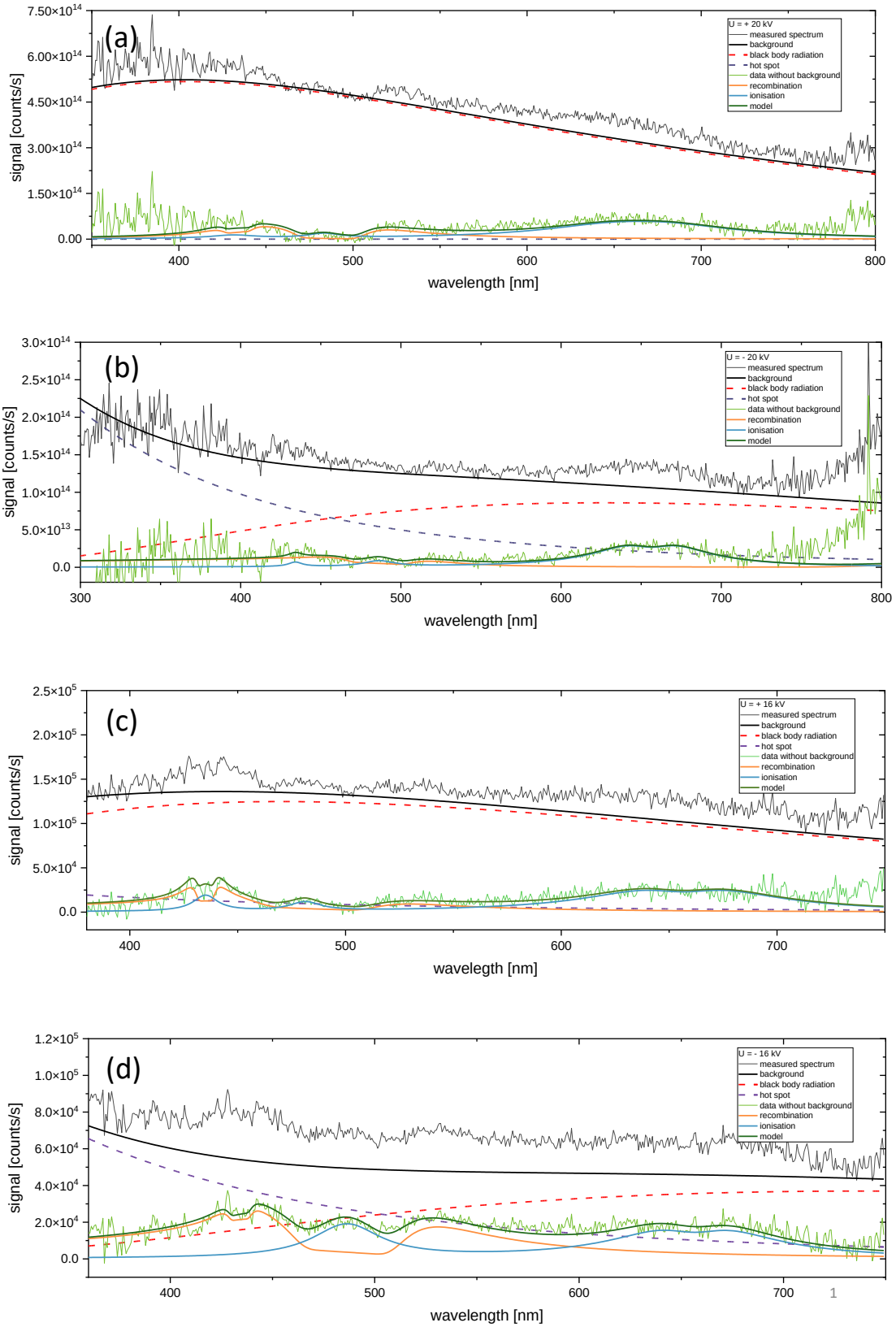

Figure 31. Analysis of the emission spectra at 4 ns after ignition for (a) $U = +20$ kV, (b) $U =$ -20 kV, (c) $U = +16$ kV and (d) $U =$ -16 kV. Continuum emission (black line) is modelled by black body radiation (red dashed lines) and a hot spot (violet dashed lines) at $T = 20\,000$ K and subtracted from the data (black). The resulting residuum (light green) can be fit with two-region model (dark green) consisting of an ionisation region (blue line) and recombination region (orange line).

A.4 ICCD Images

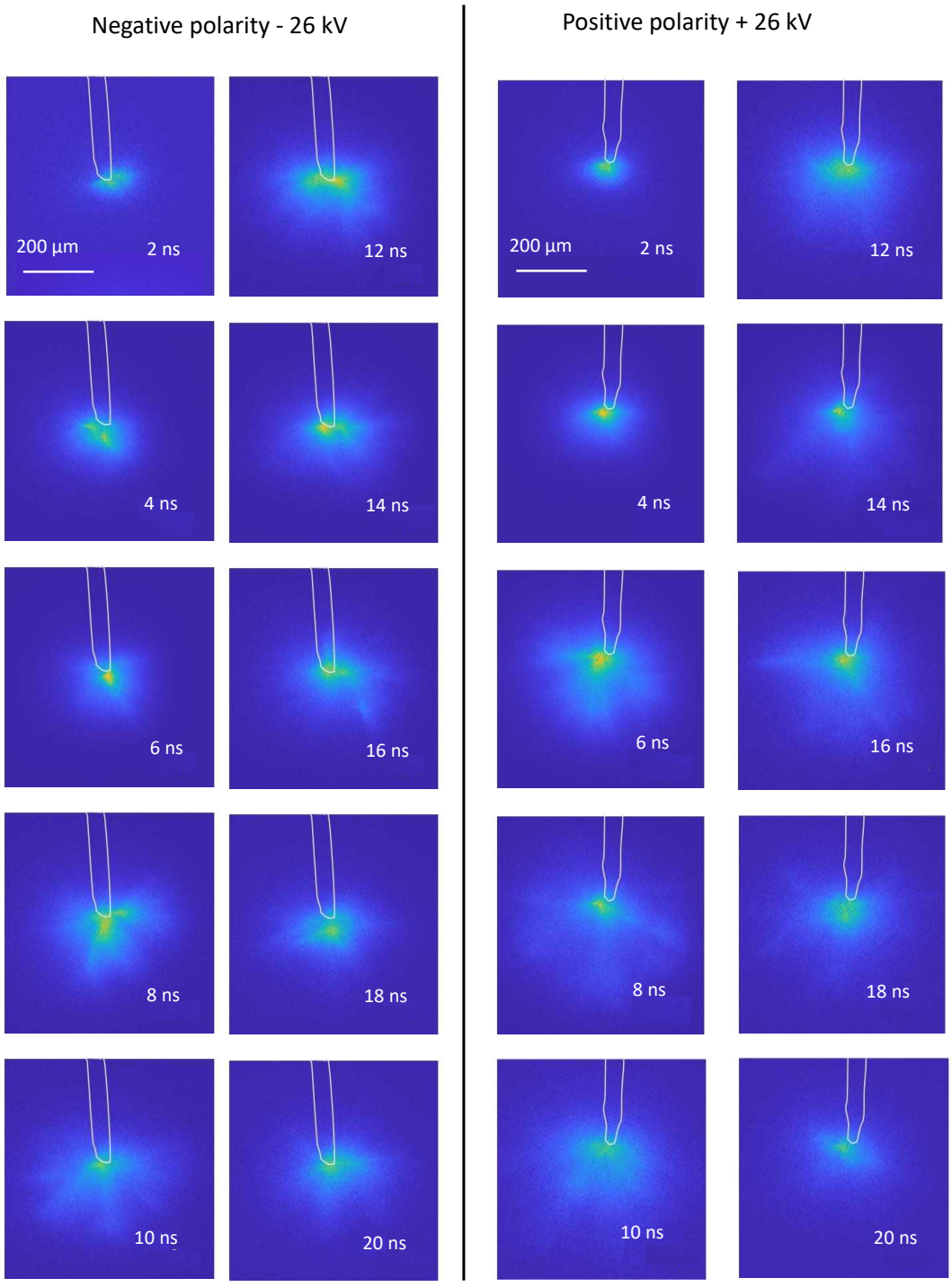

Figure 32. ICCD images of plasma emission for negative polarity (left) and positive polarity (right) at a Pt electrode. The position of the Pt electrode is reproduced by means of white lines and the time stamp for each image is in the right-hand corner. The size scale is illustrated in the top left image.

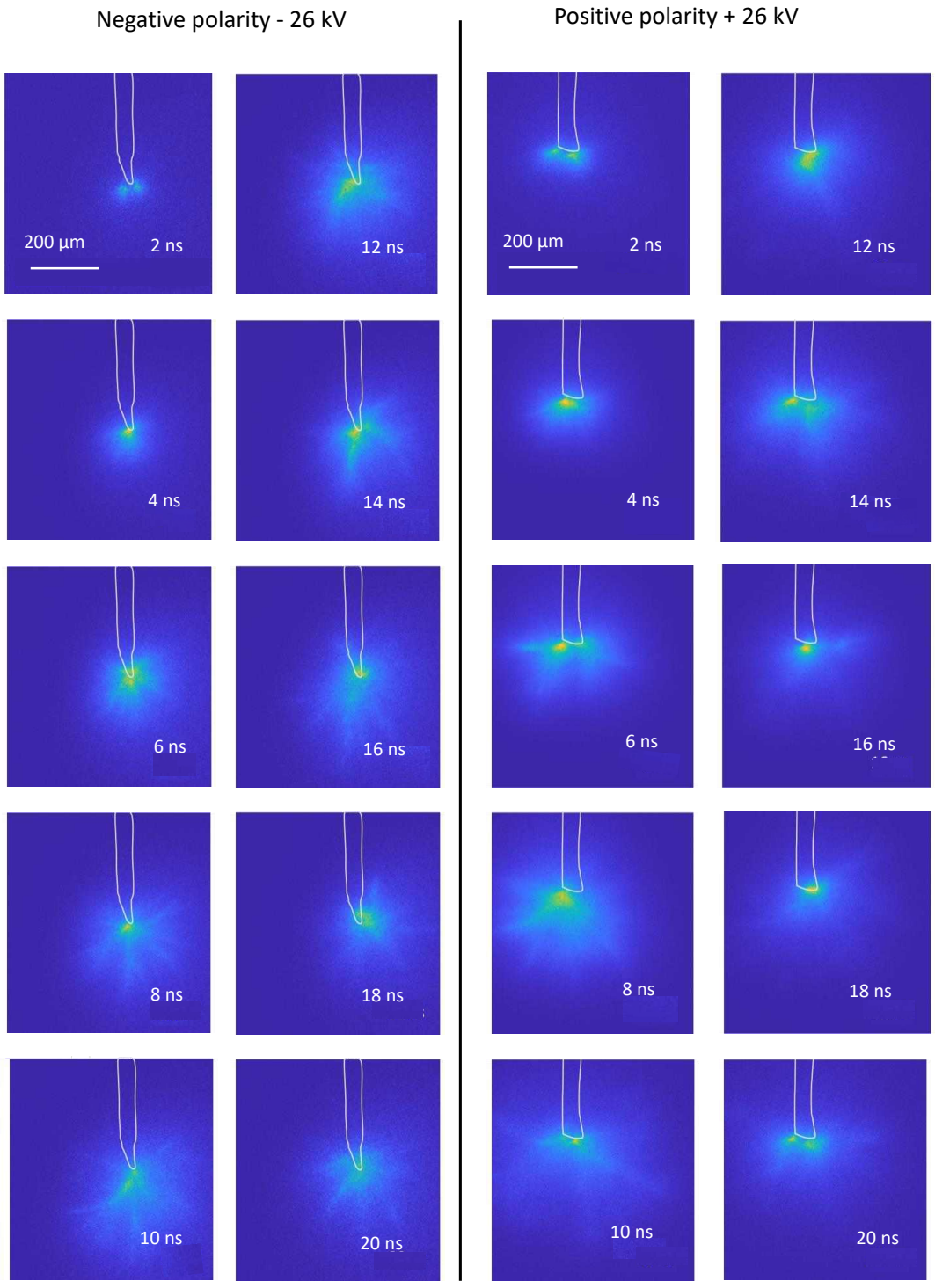

Figure 33. ICCD images of plasma emission for negative polarity (left) and positive polarity (right) at a Pt/Ir electrode. The position of the Pt/Ir electrode is reproduced by means of white lines and the time stamp for each image is in the right-hand corner. The size scale is illustrated in the top left image.

Acknowledgements

An dieser Stelle möchte ich mich bei all den tollen Menschen bedanken, die mir bei der Erstellung dieser Arbeit so tatkräftig unter die Arme gegriffen haben und mich in jeder erdenklichen Situation unterstützt haben. Ein besonderer Dank geht an:

- Prof. Dr. Achim von Keudell dafür, dass er mir die Möglichkeit gegeben hat am Lehrstuhl für Experimentalphysik 2 meine Bachelorarbeit zu erstellen und mir ein so überaus spannendes Forschungsthema angeboten hat.

- Dr. Katharina Grosse für die wirklich hervorragende Betreuung bei der Erstellung der Arbeit. Insbesondere dafür, dass sie mir mit ihrer Geduld, guten Ratschlägen und Ermutigung bei allen auftretenden Problemen geholfen hat.

- Jun. Prof. Dr. Judith Golda für die Übernahme des Zweitgutachtens dieser Arbeit.

- Dem Lehrstuhl für Werkstoffkunde, im Besonderen Felicitas Scholz und Susanne Jordans, für die Bereitstellung und Durchführung der Analyse mittels Rasterelektronenmikroskop.

- Meine Familie und Freunde, die mich immer unterstützen und für mich da sind, egal wie anstrengend dies auch mal sein mag. Besonders an Sumeja Bureković und Patrick Walkowiak für das fleißige Korrekturlesen meiner Arbeit.

- Last but not least, allen Mitgliedern des Lehrstuhls für die freundliche Aufnahme in ihre Gruppe und die interessanten Gespräche.